J. Shi, H. Zhang, X. Huang, J. Wen, G. Chen, G. Chen, A. Yu (2024) *Experimental and numerical study of gas explosion from semi-submersible platform*, **Ocean Engineering**, 295, 116958. https://doi.org/10.1016/j.oceaneng.2024.116958

Experimental and numerical study of gas explosion from semi-submersible platform

Jihao Shi[1*], He Zhang[2], Xinyan Huang[1], Jennifer Wen[3], Guoming Chen[2],

Guoxin Chen[4], Anfeng Yu[4]

[1] Department of Building Environment and Energy Engineering, The Hong Kong Polytechnic University, Kowloon, Hong Kong, China

[2] Centre for Offshore Engineering and Safety Technology, China University of Petroleum, Qingdao 266580, China

[3] Fire and Explosion Modelling Group, School of Mechanical Engineering Sciences, University of Surrey, Guildford, Surrey, GU2 7XH, UK

[4] State Key Laboratory of Safety and Control for Chemicals, SINOPEC Research Institute of Safety Engineering Co., Ltd. , Qingdao 266100, China

[*]Corresponding to shi_jihao@163.com, jihaoshi@polyu.edu.hk

Abstract:

Gas explosion can cause great structural damage to the semi-submersible platform, so understanding the gas explosion dynamics is critical to avoid the accident and its escalation to a major disaster. In this study, gas explosion experiments were conducted at a semi-submersible platform with dimensions of 3.09 m× 3.29 m × 3.46 m. Both pressure-time histories and flame evolutions were recorded from experiments. A 3D numerical model was developed in OpenFOAM and validated by experimental data. Numerical results show two flame regimes, and the transition between two flame regimes occurred close to the drilling and accommodation module, where congestion and confinement exist. The flame propagation is dominated by hydrodynamics instabilities, and it can be accelerated by congested obstacles. The transition between two flame regimes can induce the large local overpressure. For a long-distance ignition, the largest overpressure peak is located at the accommodation module of the offshore platform. For the ignition in the drilling module, a larger overpressure occurs at both the left and right edges of the main deck of offshore platform. For both ignition positions, the middle part of drilling derrick has the larger overpressure peak. This work provides theoretical support to design mitigation measures on semi-submersible platforms.

Keywords: Medium-scale offshore platform; Gas explosion; OpenFOAM; Experimental study; Numerical modeling;

1. Introduction

Compared with coal and petroleum, natural gas is a 'cleaner fuel source' in terms of pollution, and burning natural gas also produces less carbon dioxide (CO2) per energy unit. Today, natural gas has become one of the most significant transition fuels in our journey towards carbon neutrality. Deep-sea regions have a large volume of natural gas reserves, and exploration and development of such natural gas resources require the semi-submersible platform [1-3]. However, the complex and harsh marine environment would unavoidably cause the rupture of critical facilities of offshore platforms, such as tanker, pipeline, flange, etc., which results in the release and dispersion of natural gas [1, 4]. The released flammable vapor cloud, once ignited, will cause an explosion, potentially leading to many casualties, the damage of critical equipment and even collapse of the whole platform [5-7]. For example, an explosion accident of natural gas occurred from Deepwater Horizon platform in 2010, causing 11 deaths and significant environmental pollution [8]. Thus, the understanding of flame evolution, explosion mechanism and overpressure distribution from a semi-submersible platform is essential to prevent an explosion accident from escalating to a major disaster.

In the past decades, more research related to fire and explosion of offshore rigs have been conducted. For example, two joint industry projects, namely blast and fire engineering for topside structures (BFETS JIP) [9] and explosion and fire engineering of floating, production, storage and off-loading units (EFEF JIP) [10-14] have significantly expanded the knowledge domain about offshore explosion phenomenology. Gas explosion experiments from small, medium and large-scale offshore rigs were conducted [15]. In addition, a wide range of confined or unconfined gas explosion experiments were conducted with or without congested obstacles [16]. Some well-known experiments include ERGOS [17], MERGE [18], and Buxton unconfined experiments [19]. These experiments are valuable for discovering insights of congested gas explosion [20, 21]. For a semi-submersible platform, different modules contain facilities with various congestion levels. Highly congested facilities would enhance turbulence to dominate explosion evolution, while hydrodynamics instabilities play a significant role in less congested facilities. Moreover, the dynamics of gas explosion from semi-submersible platform may be different for unevenly-distributed facilities, which to date has not been fully explored.

Computational fluid dynamics (CFD) tools widely validated by experiments have been applied to investigate gas explosions from offshore facilities. Li et al., applied the well-known commercial CFD tool, namely FLACS to determine safety gap effect on gas explosion and carry out explosion risk analysis-based optimal blast wall layout design of a cylindrical FLNG platform [22, 23]. Fang et al., applied FLACS to investigate the effect of cubical obstacles on blast wave propagation from FPSO with high congestion levels [24]. Kang et al., presented a detailed review and analysis of commercial CFD tools to understand physical mechanism of explosion accidents and explosion risk analysis of offshore facilities [25]. More recently, Rosli et al., reviewed both merits and weakness of commercial CFD tools for gas explosion modeling in the chemical process industry [26]. In addition, several in-house codes based on open-source CFD tools have been developed. For instance, Shock Towards Kinetic Explosion Simulator (STOKES) has been widely validated by experiments. Because of applying Porosity Distributed Resistance (PDR) approach, STOKES has a high computational accuracy and efficiency, especially for large-scale gas explosion prediction with complex geometries [27-31]. By using PDR

approach, PDRFoam solver based on open-source toolbox, namely OpenFOAM, has also been developed and validated by gas explosion experiments with congestions [16, 32]. In addition, Xifoam is another OpenFOAM solver, and its accuracy has been validated by experiments of confined [33-35] and unconfined gas explosions [36]. However, the numerical study of gas explosion from semi-submersible platform with unevenly-distributed facilities is still very limited.

This study first conducted gas explosion tests from the semi-submersible platform with unevenly-distributed facilities, where the evolutions of pressure and flame were recorded. A 3D numerical model was developed based on Xifoam solver and then validated by experimental data. Numerical simulations were subsequently conducted to reveal dynamic characteristics of gas explosion from semi-submersible platform. The research outcomes provide valuable theoretical foundation to help design mitigation measures for gas explosion on semi-submersible platforms. The remaining paper is structured as follows, the experimental system and configurations are given in Section 2, and numerical modeling and validation are presented in Section 3. In Section 4, flame spatiotemporal propagation mechanism and overpressure distribution characteristic are discovered, and key conclusions are summarized in Section 5.

2. Experimental method

Experiment system of medium-scale semi-submersible platform was applied to conduct the premixed propane-air mixture explosion tests. This semi-submersible platform with dimensions of 3.09m× 3.29m × 3.46m includes three parts, namely topside, middle column and pontoon, as shown in Fig. 1. The topside, on which premixed propane-air mixture explosion was assumed to occur, mainly consists of drilling module and accommodation module. Unevenly distributed oil and gas facilities may act as obstacles to induce turbulence and thereby affect flame propagation on the topside. For facilities that are difficult to model, rigid steel pipes were used to reproduce their congestion level. A gas flow control system consisting of a propane tank and gas flow control device was applied to fill the propane into the topside area, which was covered by a plastic film 50 mm thick. An explosion-proof fan was used to mix propane with air to generate the flammable vapor cloud with 4.2% propane concentration. An infrared gas concentration analyzer (QGS-08C, Nanjing Xinfeng, China) monitored the concentration of the propane-air mixture at various positions to check its homogeneity.

An igniter with adjustable electric spark energy (KTD-A, Shaanxi Qinchuan, China) was applied to ignite the propane-air mixture. A high Speed Video Camera (Phantom V611, USA) was used to record flame propagation, and 8 pressure sensors (HTP400, Shaanxi Qinchuan, China) with 50 kPa pressure monitoring capacity were configured to record pressure histories at different positions. A laptop connected with dynamic pressure collection device (6400, Sichuan Chengdu Keda Shengying, China) was used to collect all the recorded data. A synchronous control device (Sichuan Chengdu Keda Shengying, China) was applied to activate the ignition and experimental data collection. Fig. 2 illustrates the gas explosion experiment system and the schematic of the semi-submersible platform.

Fig. 1 Experimental geometry of semi-submersible platform

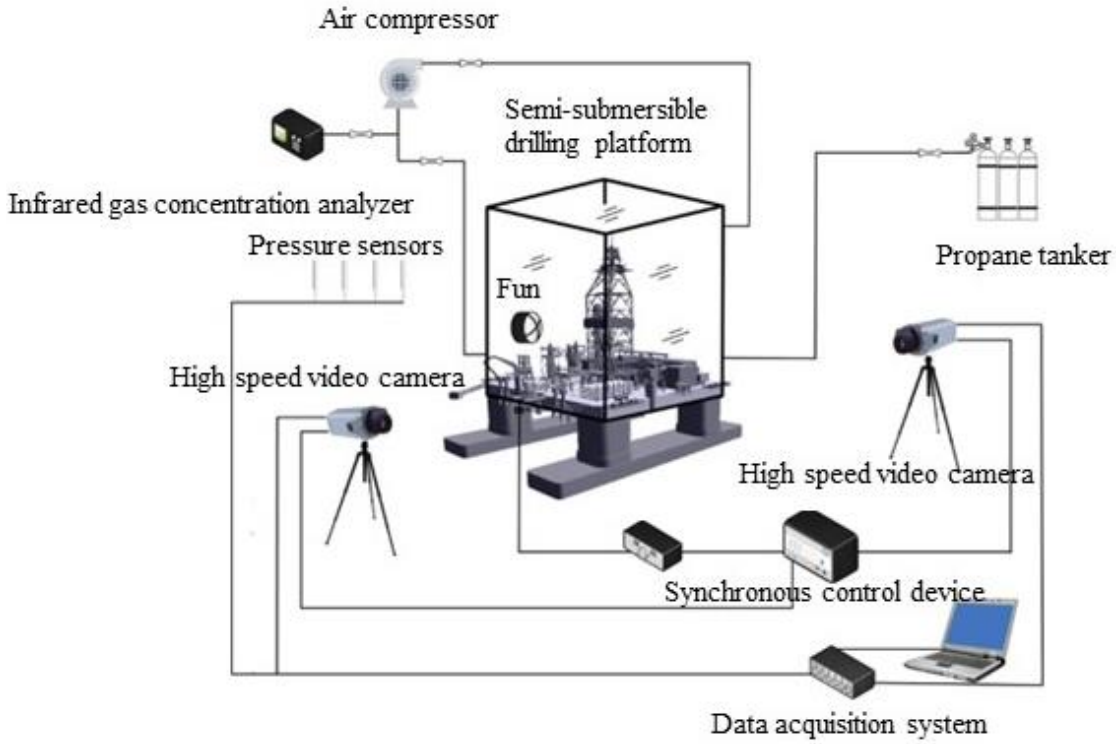

Fig. 2 Experiment system schematic of gas explosion from semi-submersible platform

The experiments include two scenarios of premixed propane-air mixture explosion tests with two different ignition positions. The 1st ignition was located at the front edge of the topside, that is, far away from the accommodation module. The 2nd ignition was located at the drilling module with a higher level of congestion. Fig. 3 shows the two ignition points on the topside of the semi-submersible platform (top view). Fig. 4 marks the locations of 8 pressure sensors on the semi-submersible platform, and their coordinates are listed in Table. 1.

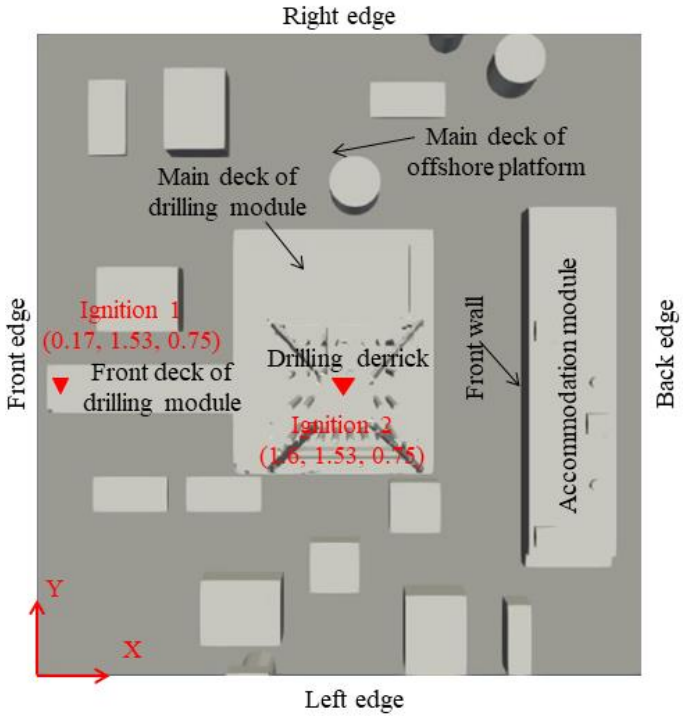

Fig. 3 Locations of two ignition points on semi-submersible platform

Table. 1 Location coordinates of 8 pressure sensors/m

Sensor	Coordinate	Sensor	Location
MP1	(0.17,1.35,0.72)	MP 5	(1.05,1.28,0.82)
MP 2	(1.25,1.35,1.47)	MP 6	(1.53,1.3,1.57)
MP 3	(2,1.28,0.85)	MP 7	(1.8,1.3,1.57)
MP 4	(2.41,1.38,0.83)	MP 8	(2.87,0.1,0.4)

Noting that MP1 presents the 1st pressure sensor.

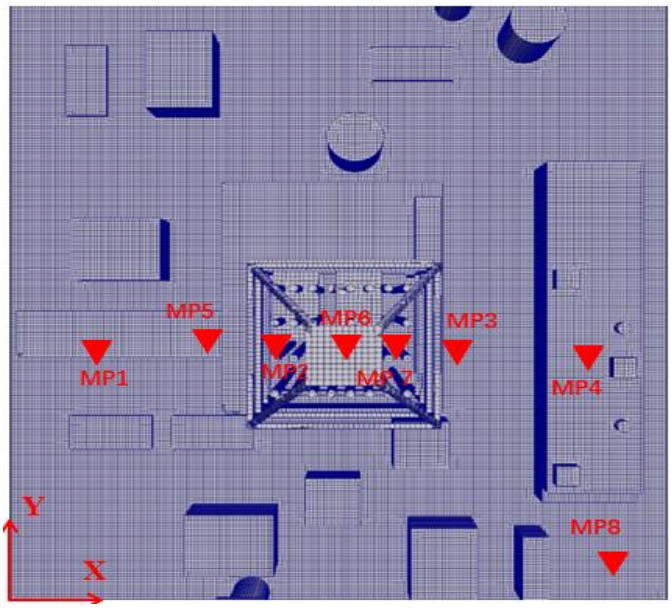

Fig. 4 Locations of 8 pressure sensors on semi-submersible platform

3. Numerical method

3.1. Numerical models

Numerical modeling of gas explosion from a semi-submersible platform was conducted by using OpenFOAM. The major assumptions include Reynolds Averaged Navier Stokes (RANs) simplification, $k-\varepsilon$ turbulence model and flame wrinkling combustion model.

(1) RANs equations

Gas explosion from a semi-submersible platform is essentially a turbulent premixed combustion with unevenly-distributed obstacles. Compressible Navier-Stokes equations could describe the conservation of mass, momentum, energy and chemical species of this turbulent premixed combustion. By introducing the Reynolds averaging procedure to density and pressure, and mass averaging to the remaining flow variables in the compressible Navier-Stokes equations, RANs equations could be determined. The Mass-averaged equation for the mass conservation can be expressed as:

$$\frac{\partial \bar{\rho}}{\partial t}+\frac{\partial}{\partial x_i}(\bar{\rho}\tilde{u}_i)=0 \tag{1}$$

where $\bar{\rho}$ is Reynolds-averaged density, t is time, $\tilde{u}_i$ is mass-averaged velocity of i component. Furthermore, the Mass-averaged equation for conservation of momentum can be written as:

$$\frac{\partial}{\partial t}(\bar{\rho}\tilde{u}_i)+\frac{\partial}{\partial x_j}(\bar{\rho}\tilde{u}_i\tilde{u}_j)=-\frac{\partial \bar{p}}{\partial x_i}+\frac{\partial}{\partial x_j}(\bar{\tau}_{ij}-\bar{\rho}u_i''u_j'')+\bar{\rho}f_i \tag{2}$$

where $\bar{\tau}_{ij}$ can be expressed as:

$$\bar{\tau}_{ij}=\mu\left[\left(\frac{\partial \tilde{u}_i}{\partial x_j}+\frac{\partial \tilde{u}_j}{\partial x_i}\right)-\frac{2}{3}\delta_{ij}\frac{\partial \tilde{u}_k}{\partial x_k}\right] \tag{3}$$

In addition, the Mass-averaged equation of conservation of enthalpy $\tilde{h}$ can be written as:

$$\frac{\partial}{\partial t}(\bar{\rho}\tilde{h})+\frac{\partial}{\partial x_j}(\bar{\rho}\tilde{h}\tilde{u}_j)=\frac{\partial \bar{p}}{\partial t}+\tilde{u}_j\frac{\partial \bar{p}}{\partial x_j}+\frac{\partial}{\partial x_j}\left(\bar{\rho}\overline{D_r}\frac{\partial \tilde{h}}{\partial x_j}-\bar{\rho}u_j''h''\right)+\bar{\dot{Q}}+\bar{S}_h, \tag{4}$$

where $\bar{S}_h$ is the source term, which accounted for the losses due to friction in the fluid inside the control volume, chemical and potential energy, $\overline{D_r}$ is the turbulence diffusion coefficients, $\bar{\rho}u_j''h''$ is the unresolved enthalpy fluxes, and $\bar{\dot{Q}}$ is the heat produced due to external sources.

The Mass-averaged equation for chemical species conservation can be expressed as

$$\frac{\partial}{\partial t}(\bar{\rho}\tilde{Y}_r)+\frac{\partial}{\partial x_j}(\bar{\rho}\tilde{u}_j\tilde{Y}_r)=\frac{\partial}{\partial x_j}\left(\bar{\rho}\overline{D_r}\frac{\partial \tilde{Y}_r}{\partial x_j}\right)-\frac{\partial}{\partial x_j}(\bar{\rho}u_j''Y_r'')+\bar{R}_r, \tag{5}$$

where R_r is the rate of production or consumption of the chemical species r in combustion.

The mass-weighted Reynolds stresses $\bar{\rho}u_i''u_j''$ in Eq. (2), the unresolved enthalpy fluxes $\bar{\rho}u_j''h''$ in Eq. (4), and species fluxes $\bar{\rho}u_j''Y_r''$ in Eq. (5) are unknown and required to be modeled by turbulence model in order to close the RANs equations.

(2) $k-\varepsilon$ turbulence model

One of the widely-accepted two-equation turbulence model, namely $k-\varepsilon$ turbulence model is applied to model the above unsolved terms. $k-\varepsilon$ turbulence model can be expressed as follows:

$$\frac{\partial}{\partial t}(\bar{\rho}k)+\frac{\partial}{\partial x_j}(\bar{\rho}\tilde{u}_j k)=\frac{\partial}{\partial x_j}\left[\left(\mu+\frac{\mu_t}{\sigma_k}\right)\frac{\partial k}{\partial x_j}\right]+P_k-\bar{\rho}\varepsilon, \quad (6)$$

$$\frac{\partial}{\partial t}(\bar{\rho}\varepsilon)+\frac{\partial}{\partial x_j}(\bar{\rho}\tilde{u}_j \varepsilon)=\frac{\partial}{\partial x_j}\left[\left(\mu+\frac{\mu_t}{\sigma_e}\right)\frac{\partial \varepsilon}{\partial x_j}\right]+C_{\varepsilon 1}\frac{\varepsilon}{k}P_k-C_{\varepsilon 2}\frac{\varepsilon^2}{k}, \quad (7)$$

where k is turbulence energy, ε is dissipation of turbulence energy, σ_k is the turbulent Prandtl numbers for k and σ_ε is the Prandtl numbers for ε. The source term, P_k, can be expressed as:

$$P_k=-\bar{\rho}u_i''u_j''\frac{\partial \tilde{u}_\iota}{\partial x_j}, \quad (8)$$

where the Reynolds stresses $\bar{\rho}u_i''u_j''$, can be determined using the Boussinesq approximation as follows:

$$\bar{\rho}u_i''u_j''=-\mu_t\left(\frac{\partial \tilde{u}_i}{\partial x_j}+\frac{\partial \tilde{u}_j}{\partial x_i}-\frac{2}{3}\delta_{ij}\frac{\partial \tilde{u}_l}{x_l}\right)+\frac{2}{3}\bar{\rho}k, \quad (9)$$

In this turbulence model, the turbulence viscosity μ_t can be expressed as:

$$\mu_t=C_\mu\bar{\rho}\frac{k^2}{\varepsilon} \quad (10)$$

The unsolved turbulent species in Eq. (4) and enthalpy fluxes in Eq. (5) can be closed using a gradient-diffusion hypothesis:

$$\bar{\rho}u_j''Y_r''=-\frac{\mu_t}{Sc_{tk}}\frac{\partial \tilde{Y}_r}{\partial x_j} \quad (11)$$

$$\bar{\rho}u_j''h''=-\frac{\mu_t}{\mathrm{Pr}_t}\frac{\partial \tilde{h}}{\partial x_j} \quad (12)$$

where Sc_{tk} is the turbulent Schmidt number for species k and Pr_t is the turbulent Prandtl number.

(3) Flame wrinkling combustion model

In premixed combustion, the flame propagates from the burned to unburned gases and this flame propagation can be denoted by the progress variable, c. This progress variable taking values 0 and 1 in fresh and fully burned gas regions, respectively, and between 0 and 1 across the flame which describes the progress of the reaction. This progress variable c can be calculated in terms of temperature as follows:

$$c=\frac{T-T_u}{T_b-T_u} \quad (13)$$

where T is the temperature, and the subscripts u and b represent the unburned and burned gases. The thermophysical process of flame propagation is represented by the transport equation for the density-weighted mean regress variable $b=1-c$, and can be expressed as:

$$\frac{\partial}{\partial t}(\bar{\rho}\tilde{b})+\nabla\cdot(\bar{\rho}\tilde{u}\tilde{b})-\nabla\cdot\left(\frac{\mu_t}{Sc_t}\nabla\tilde{b}\right)=-\overline{\rho_u}S_L\Xi|\nabla\tilde{b}| \quad (14)$$

where $Sc_t=\frac{\mu}{\rho\mathcal{D}}$is the turbulent $Schmidt$ number , $\mathcal{D}$ is the diffusion coefficient, ρ_u is the unburned mixture density, S_L is the laminar flame speed which can be modeled as a function of fuel mixture,

equivalence ratio, pressure, and temperature of the unburnt gas as follows:

$$S_L(\phi, T_u, p_u) = S_L^o \left(\frac{T_u}{T_o}\right)^{\alpha} \left(\frac{p}{p_o}\right)^{\beta} \quad (15)$$

where S_L^o is the laminar flame speed, also known as unstrained laminar flame speed, measured at initial/room conditions, i.e., at $T_u = T_o$ and $p = p_o$, for a given equivalence ratio ϕ, and α and β are constants or mixture strength-dependent terms. Gülder [28] proposed the empirical expression to represent the laminar flame speed at room conditions as a function of equivalence ratio:

$$S_L^o = ZW\phi^{\eta}\exp[-\xi(\phi - 1.075)^2] \quad (16)$$

where $Z = 1$ for single constituent fuels, and W, η, and ξ are constants specified for each fuel. In Eq. (14), Ξ represents the sub-grid flame wrinkling, which can be defined as the ratio of turbulent and laminar flame speed. Ξ can be computed by using the transport equation as follows:

$$\frac{\partial \Xi}{\partial t} + U_s \cdot \nabla \Xi = G\Xi - R(\Xi - 1) + (\sigma_s - \sigma_t)\Xi \quad (17)$$

where U_s is the average velocity of the flame surface, σ is the resolved strain rate. The first and second terms on the right-hand side of Eq. (15), respectively, are the sub-grid turbulent generation and removal rates. The rate coefficients G and R, respectively, are modeled as:

$$G = R\frac{\Xi_{eq} - 1}{\Xi eq},\ R = \frac{0.28}{\tau_\eta}\frac{\Xi_{eq}^*}{\Xi_{eq}^* - 1}, \quad (18)$$

where τ_η is the Kolmogorov time scale and Ξ_{eq} is the equilibrium Ξ given by the following simple algebraic expression.

$$\Xi_{eq} = 1 + 2\lambda_1(0.5 - b)\left(\Xi_{eq}^* - 1\right) \quad (19)$$

The equilibrium wrinkling at the Kolmogorov turbulence length scale, Ξ_{eq}^*, can be expressed by the algebraic equation of the sub-grid flame wrinkling proposed by Gülder as follows:

$$\Xi_{eq}^* = 1 + \lambda_2 \left(\frac{u'}{S_L}\right)^{1/2} Re_\eta \quad (20)$$

where Re_η is the Reynolds number based on the Kolmogorov length scale. λ_1 and λ_2 are empirical constants which could be efficiently calibrated by our in-house developed inversely-solving code by connecting Python deep learning module with OpenFOAM. By using the experimental data as benchmark, we determined λ_1=1 and $\lambda_2 = 1.1$, respectively, in this study.

3.2. Numerical configurations

The numerical configurations, such as numerical domain, initial and boundary conditions, and grid sensitivity analysis, are presented in this section. The dimensions of the numerical domain were 5 m in length, 5 m in width, 5 m in height, respectively. The core numerical domain was occupied by a CAD geometry of the offshore platform. The dimensions of this CAD geometry were the same as the experimental one. Two groups of boundary conditions, namely wall boundary and open boundary, were configured in the numerical domain. Wall boundary condition was used in terms of the CAD geometry of the offshore platform. An open boundary condition was applied to the whole numerical domain to minimize its reflection effect on premixed propane-air mixture explosion in the core numerical domain.

Table. 2 shows the initial variables setting of the internal field, wall and open boundaries of the numerical domain. Note that the initial value of Ft, i.e., the mass fraction of propane, was configured as 0.6 for the core numerical domain. This is to say the premixed propane-air mixture with 4.2% propane concentration only exists on the topside of the offshore platform, which is the same as the experimental setup.

Table. 2 Initial configurations of InternalField and boundary variables

Variable	InternalField	Wall boundary	Open boundary
T	293	fixedValue 293	inletOutlet 293
Tu	293	fixedValue 293	inletOutlet 293
p	101325	zeroGradient	totalPressure
U	(0,0,0)	noSlip	inletOutlet (0,0,0)
Su	0.434	inletOutlet	zeroGradient
Xi	1	zeroGradient	zeroGradient
b	1	zeroGradient	zeroGradient
Ft	0.06	zeroGradient	inletOutlet 0.06
nut	0	nutkWallFunction	calculated
alphat	0	calculated	calculated
k	0.001	kqRWallFunction 0	inletOutlet
epsilon	0.001	epsilonWallFunction 0	inletOutlet

Two mesh utilities in OpenFOAM toolbox, namely blockMesh and snappyHexMesh were applied to generate the structured mesh of the numerical domain. We first used blockMesh to generate a background mesh with uniform cell size across the whole numerical domain and then applied snappyHexMesh to snap the uniformed mesh to offshore platform geometry and accordingly refine the mesh size of core numerical domain. The premixed propane-air mixture explosion was numerically solved by using the solver XiFoam. The convective term was discretized using the upwind scheme. The diffusion term used a central difference scheme. The time advancement was addressed using first-order Euler. Pressure-velocity coupling was addressed via PIMPLE algorithm. The iteration time step size was set to be adjustable according to local grid size with maximum Courant number=0.3 to ensure stability, as well as efficiency of numerically solving. The converged residuals for energy equations, progress variable equations and momentum equations were set less than 1×10^{-6}, 1×10^{-4} and 1×10^{-5}, respectively. The computer with the configuration of 252 GB RAM, Intel Xeon (R) Gold 6226 R CPU was applied, and each simulation in parallel on 16 distributed processors requires about 40 hours.

Grid sensitivity analysis was conducted to ensure the simulation convergence. Taking the 1st ignition position as an example to illustrate the result of grid sensitivity analysis. We considered three grid configurations, including 4 million, 7 million and 9 million of grids, respectively. The initial sizes of uniformed mesh under 4 million, 7 million and 9 million of grids are 0.30 m, 0.25 m and 0.22 m, respectively. A spatial encryption level of 4 was then applied to snap the uniformed mesh to offshore geometry and accordingly refine the mesh size of core numerical domain. Fig. 5 shows the mesh configuration of the whole offshore platform under 9 million of grids. Fig. 6 demonstrates variations of

predicted maximum overpressure under different numbers of grids for the 1st ignition position. There is a significant difference in predicted maximum overpressures between 4 million and 7 million grids. With further increasing the number of grids from 7 million to 9 million, this difference becomes minimal. This indicates the simulation convergence under 9 million grids. We then performed the validation and simulations as follows by using this developed numerical model under 9 million grids.

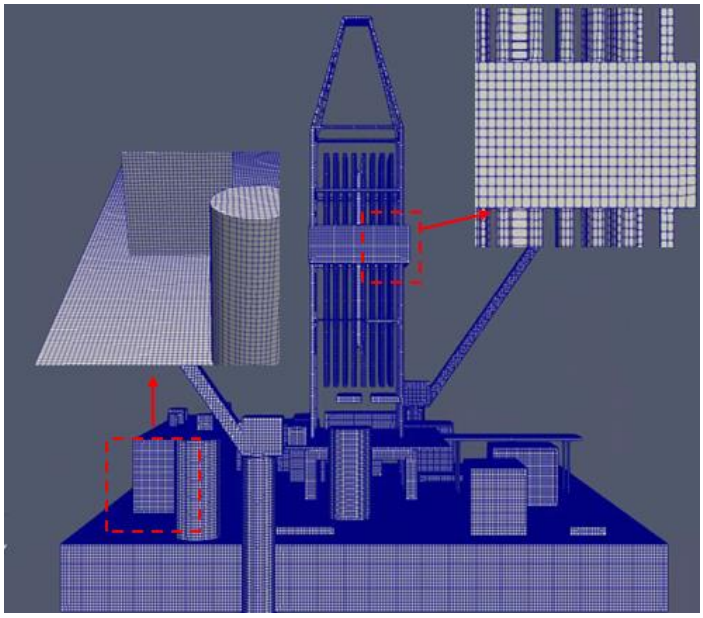

Fig. 5 Numerical mesh configuration of the whole platform under 9 million of grids

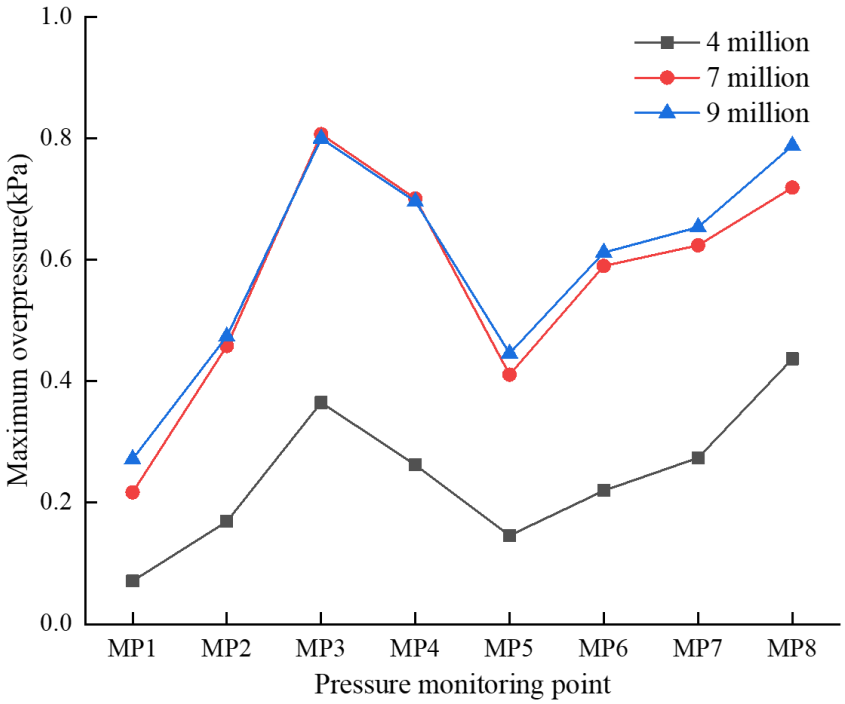

Fig. 6 Grid sensitivity analysis under the 1st ignition position condition

3.3. Model validation

The experimentally recorded flame propagation sequences by using High Speed Video Camera were first used to validate the developed numerical model under 9 million of grids. Fig. 7 shows the

comparison of flame propagation between the experiment and simulation under the 1st ignition point. From it, one may see the experimental flame propagates close to the drilling module at t=0.20s after ignition. The flame propagates to the middle of the drilling module at about t=0.28s and then to the accommodation module at about t=0.30s. At about t=0.32s, most of the platform topside is occupied by combustion flame. In addition, one may see the predicted flame propagation agrees well with the experimental observation under the 1st ignition point. The difference in the flame shape is small, considering it is difficult to capture the experimental flame propagation front clearly with the high-speed camera.

Fig. 8 compares the flame propagation between the experiment and simulation under the 2nd ignition point. The experimental explosion flame covers the main deck of the drilling module at t=0.18s after ignition. The flame propagates to the front and back edges of the whole platform topside at about t=0.22s. The platform topside is almost occupied by the experimental flame at t=0.24s. The numerical flame propagation speed is a little faster than the experimental one. The difference may be attributed to the fact that (1) the hollow pipes exist in the drilling module, and plastic films were applied to cover both the top and bottom of these hollow pipes to avoid flame propagation inside pipes; and (2) during the experiments, these plastic films were raptured, and the confined space of pipes accelerated the flame propagation. However, the numerical model could not model these detailed processes.

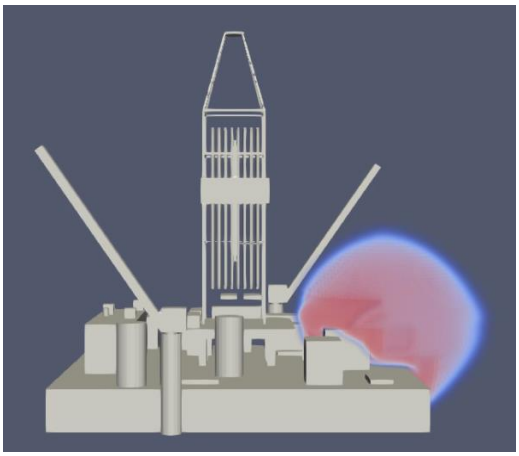

t=0.2s

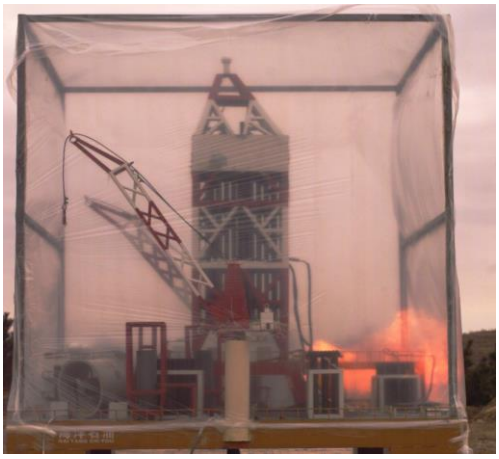

t=0.2s

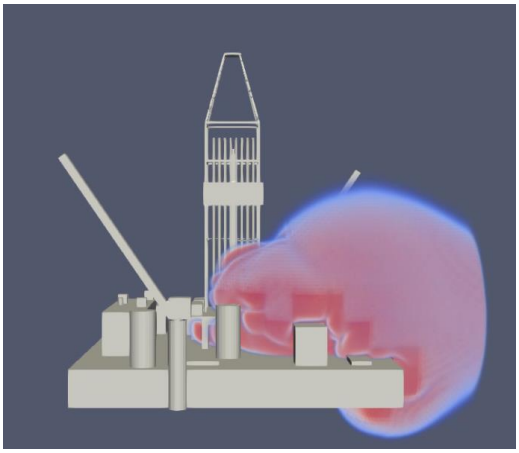

t=0.28s

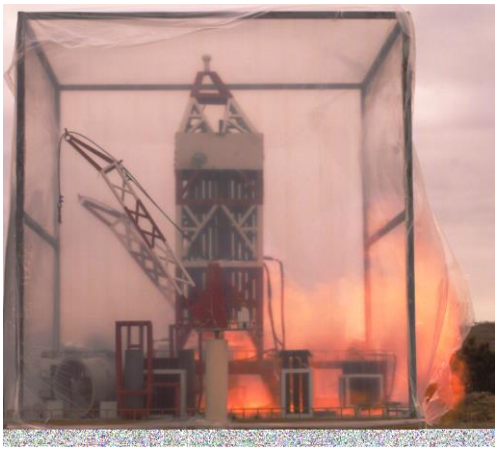

t=0.28s

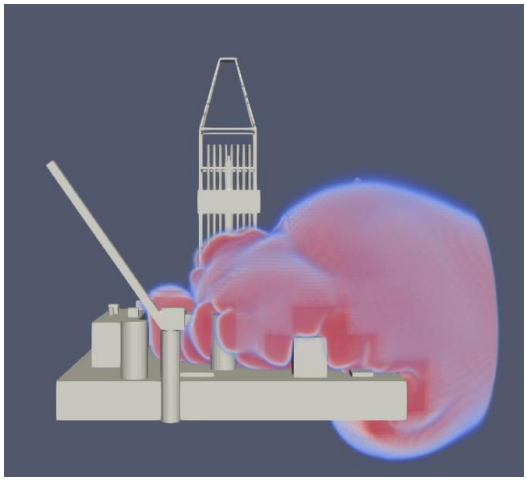

t=0.3s

t=0.3s

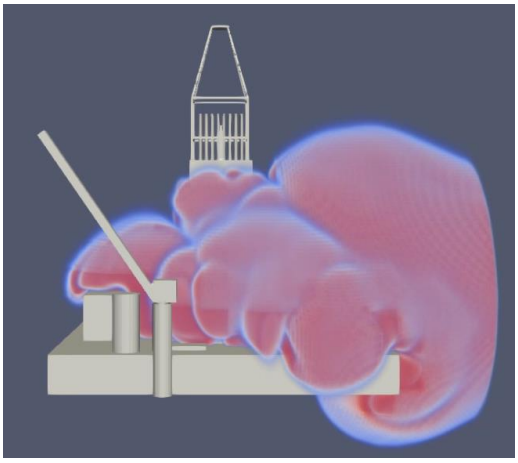

t=0.32s

t=0.32s

Fig. 7 Comparison of flame propagation between experiment and simulation under the 1st ignition point

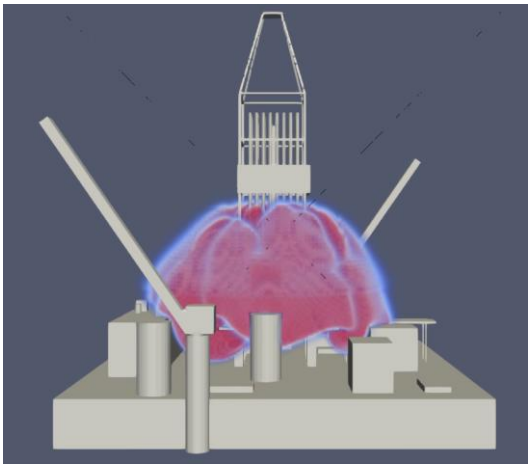

t=0.18s

t=0.18s

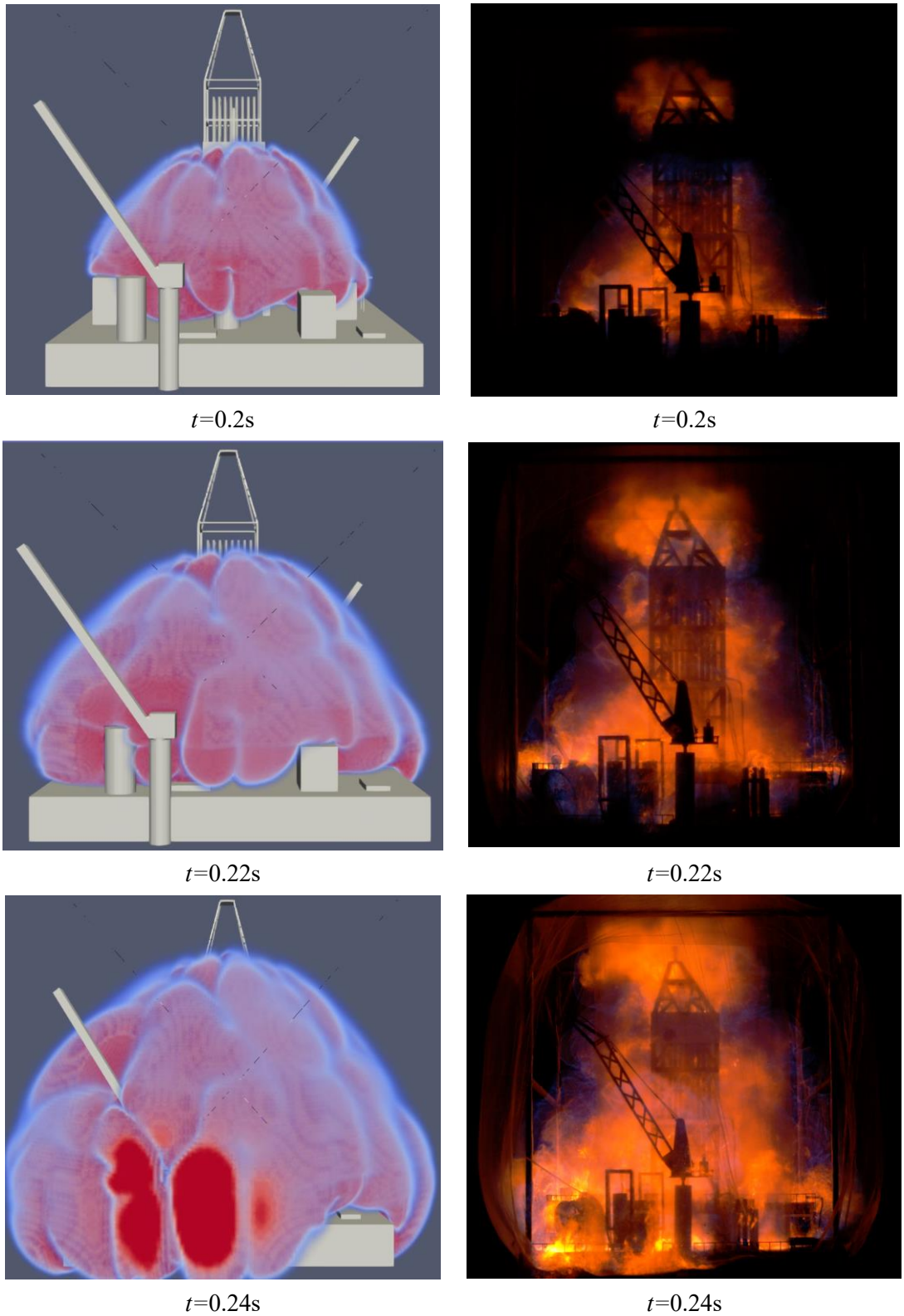

t=0.2s *t*=0.2s

t=0.22s *t*=0.22s

t=0.24s *t*=0.24s

Fig. 8 Comparison of flame propagation between experiment and simulation under the 2nd ignition point

The experimental pressure-time histories recorded by 8 pressure sensors were then used to validate the developed numerical model under 9 million grids. Fig. 9 compares the pressure history between the experiment and simulation for the 1st ignition point. Clearly, all cases contain two overpressure peaks. The first overpressure peak occurs at about *t*=0.30s, and the second peak arises at about *t*=0.35s. In

addition, the first peak values are generally larger than the second ones. Furthermore, our developed numerical model can predict two overpressure peaks at the timeslot corresponding to the experiment under the 1st ignition point. Note that in terms of MP8, the numerical overpressure peak occurs a little bit later compared to the experimental data. This may be attributed to the constraints of plastic film to the flame propagation at the position of MP8.

Fig. 10 compares the pressure history between the experiment and simulation under the 2nd ignition point. Most of the experimental pressure-time histories have two overpressure peaks. The first peaks happen before t=0.20s, and the second peaks occur after t=0.20s, where the time gap between the two peaks is very small. Our numerical model can predict the values of two overpressure peaks accurately, although predicted overpressure peaks occur later than experiments. This is expected because the experimental flame propagation is faster than the numerical one in Fig. 8. Comparison of maximum overpressures at all monitoring points between experiment and simulation under two ignition positions is demonstrated in Fig. 11. All the points are located between +/- 25% confident interval indicating the predictive accuracy of our numerical model for gas explosion from semi-submersible platform under 9 million of grids[37].

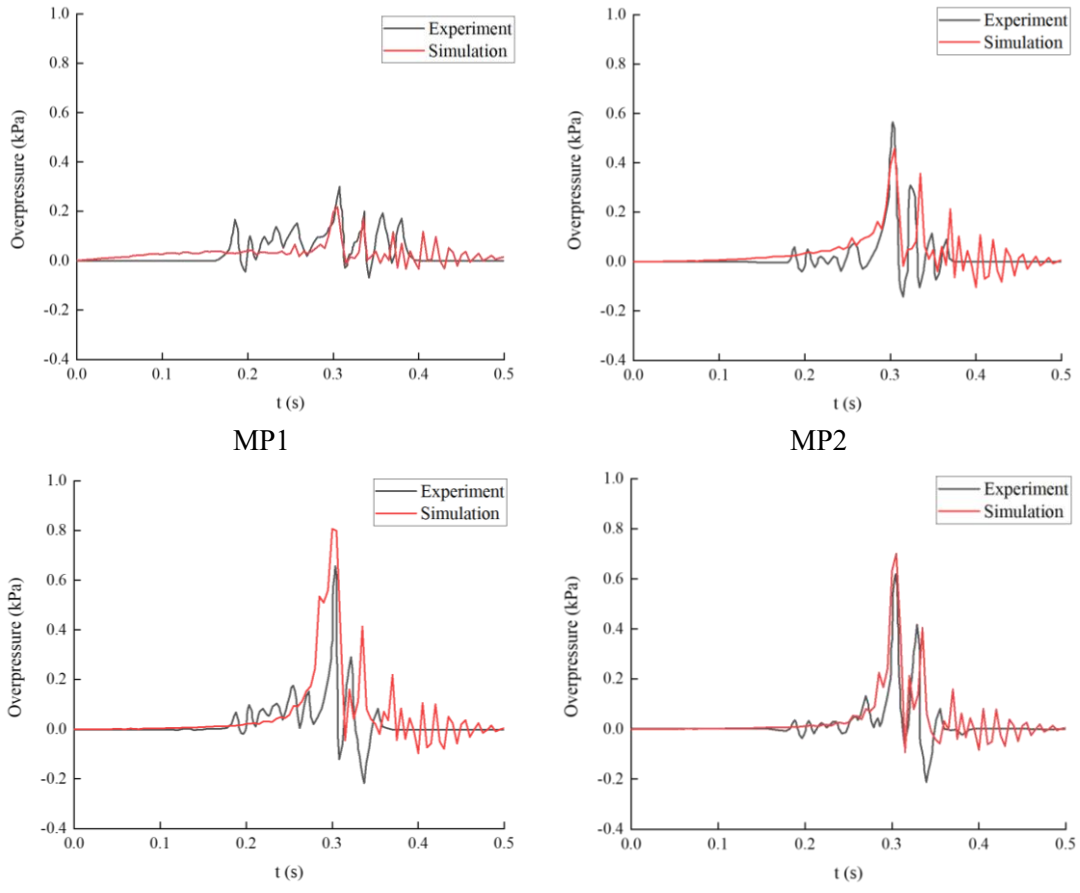

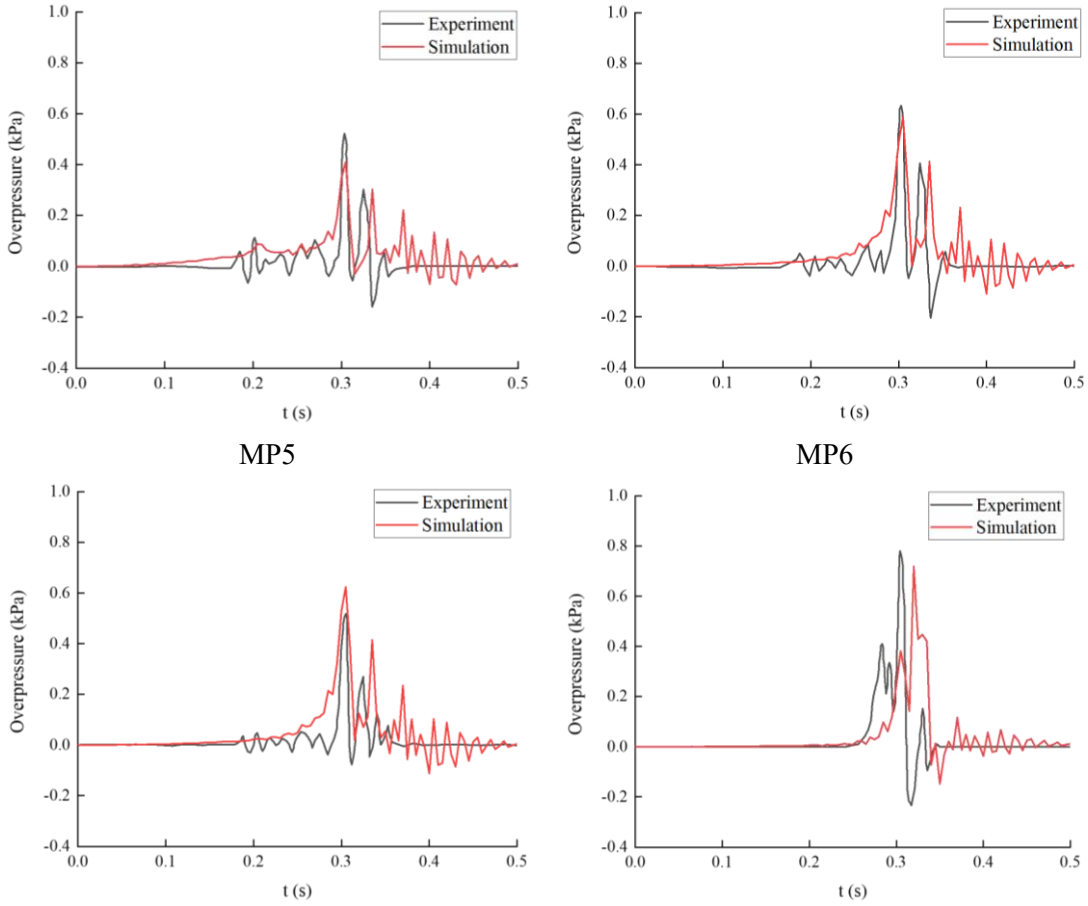

Fig. 9 Comparison of pressure histories between experiment and simulation under the 1st ignition point

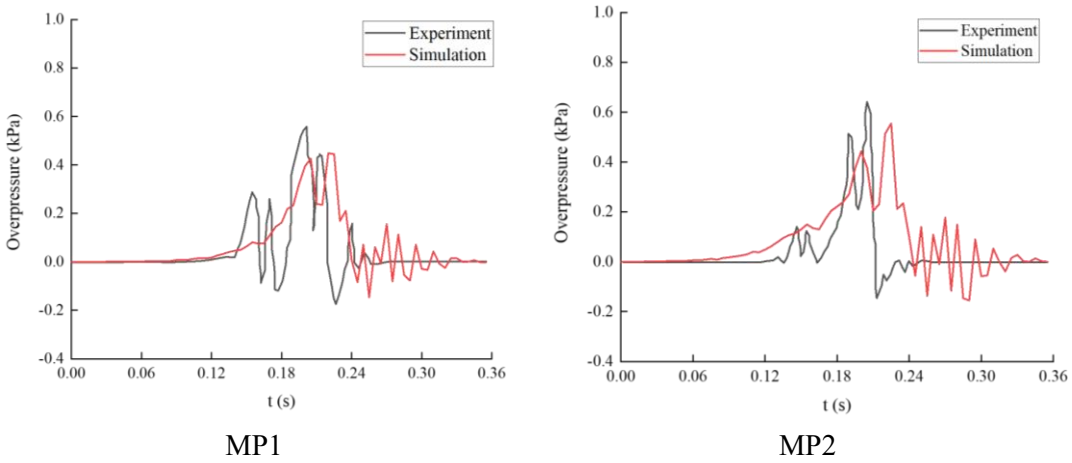

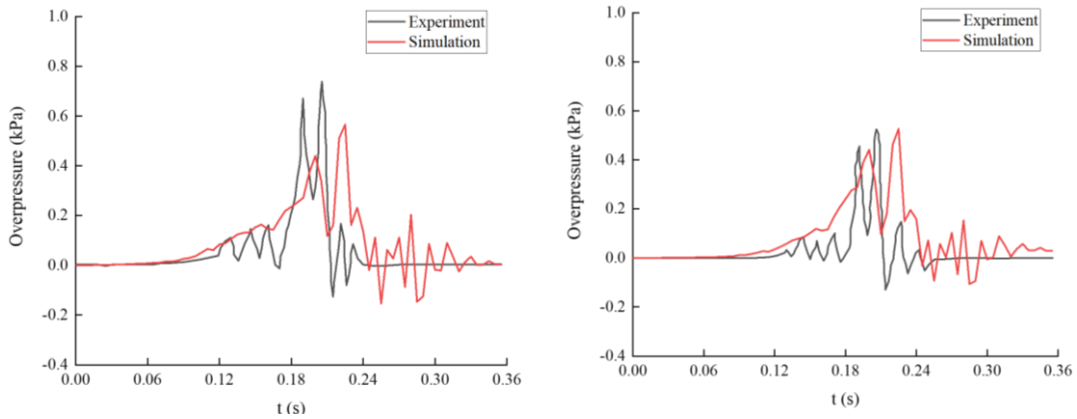

MP3

MP4

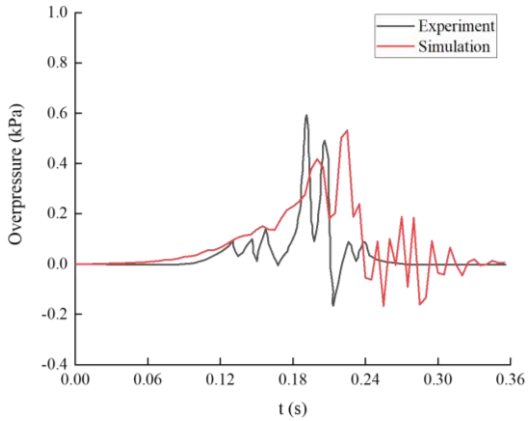

MP5

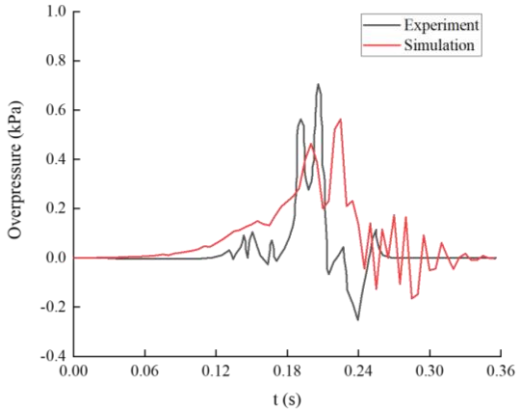

MP6

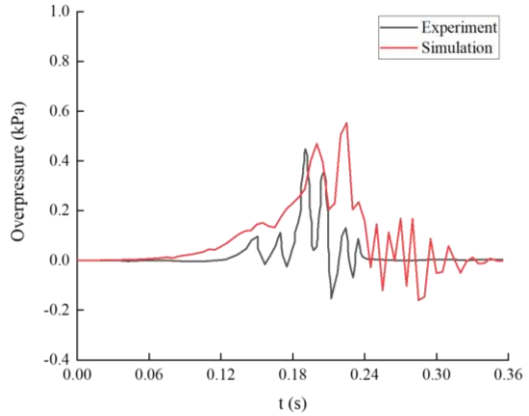

MP7

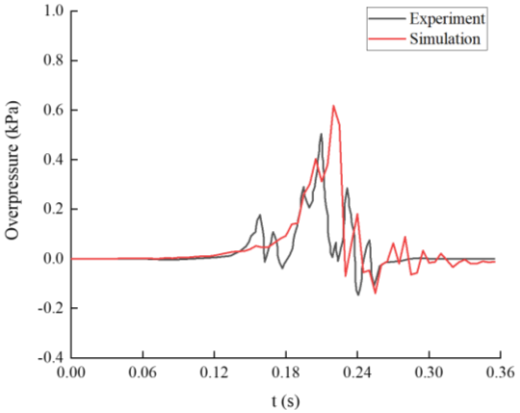

MP8

Fig. 10 Comparison of pressure histories between experiment and simulation under the 2nd ignition point

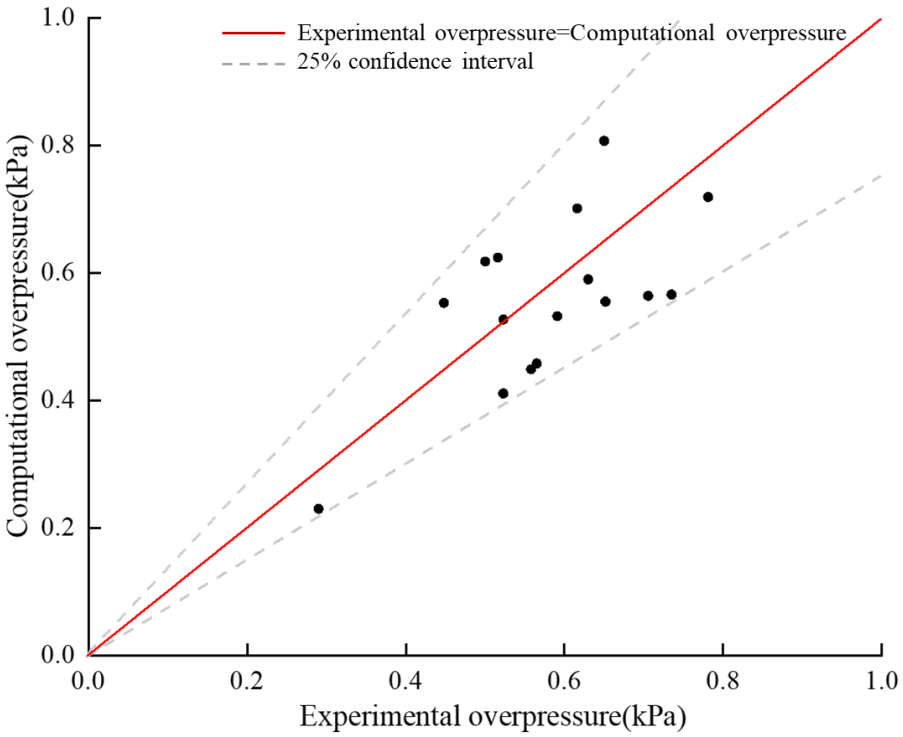

Fig. 11 Comparison of maximum overpressures at all monitoring points between experiment and simulation

4. Mechanism and characteristic of gas explosion from semi-submersible platform

4.1. Flame spatiotemporal propagation mechanism

(1) The 1st ignition point

Taking the XZ slice of 1st ignition position as an example to investigate the flame propagation mechanism. Fig. 12 shows the exampled XZ slice, including five flame propagation directions, namely a, b, c, d and e directions. For direction a, the flame propagates through the area confined by the platform main deck, drilling module deck and accommodation module. For direction b, the flame propagates through the area of the drilling module containing congested drilling risers. There are no obstacles in both directions c and e, while in direction d, the flame propagates through the whole drilling module containing congested obstacles. Note that Fig. 12 demonstrates the start points with coordinates of 5 directions as well.

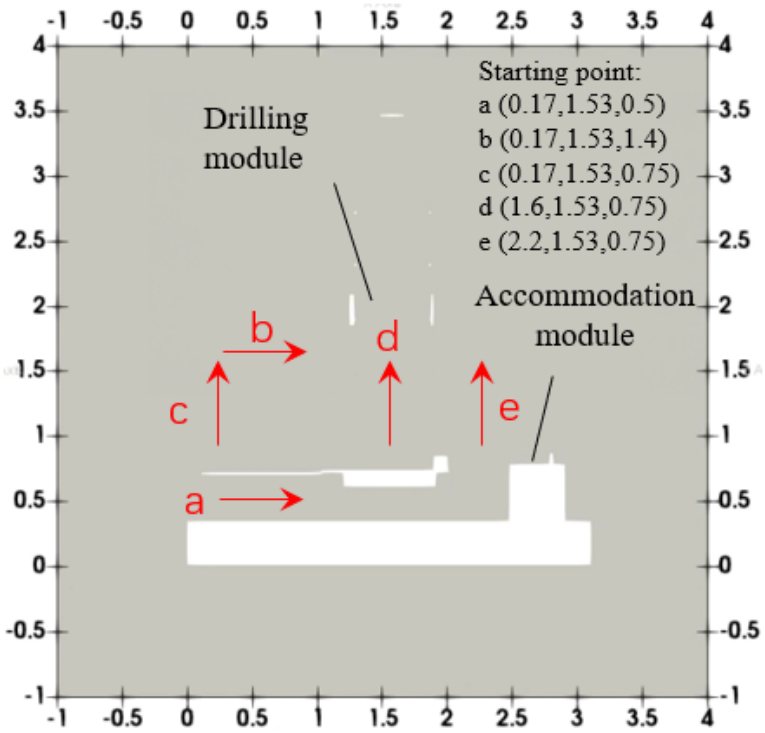

Fig. 12 5 exampled directions of flame propagation at XZ slice of the 1st ignition position

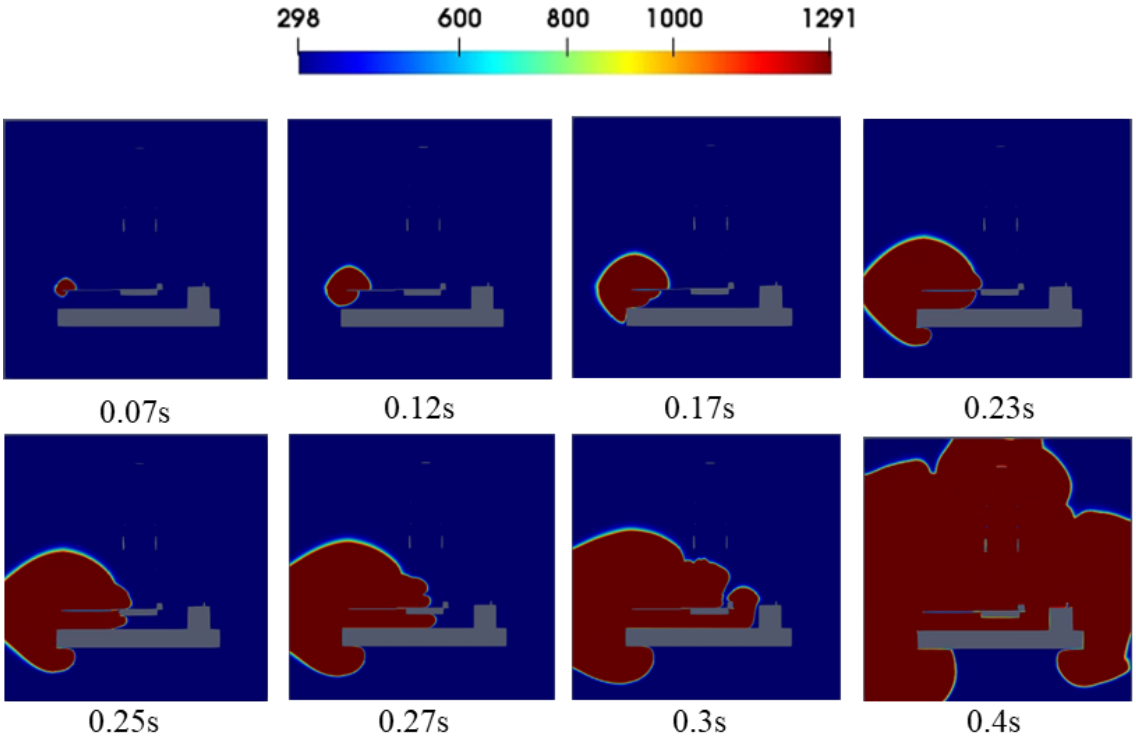

Fig. 13 Flame front propagation of XZ slice of the 1st ignition position

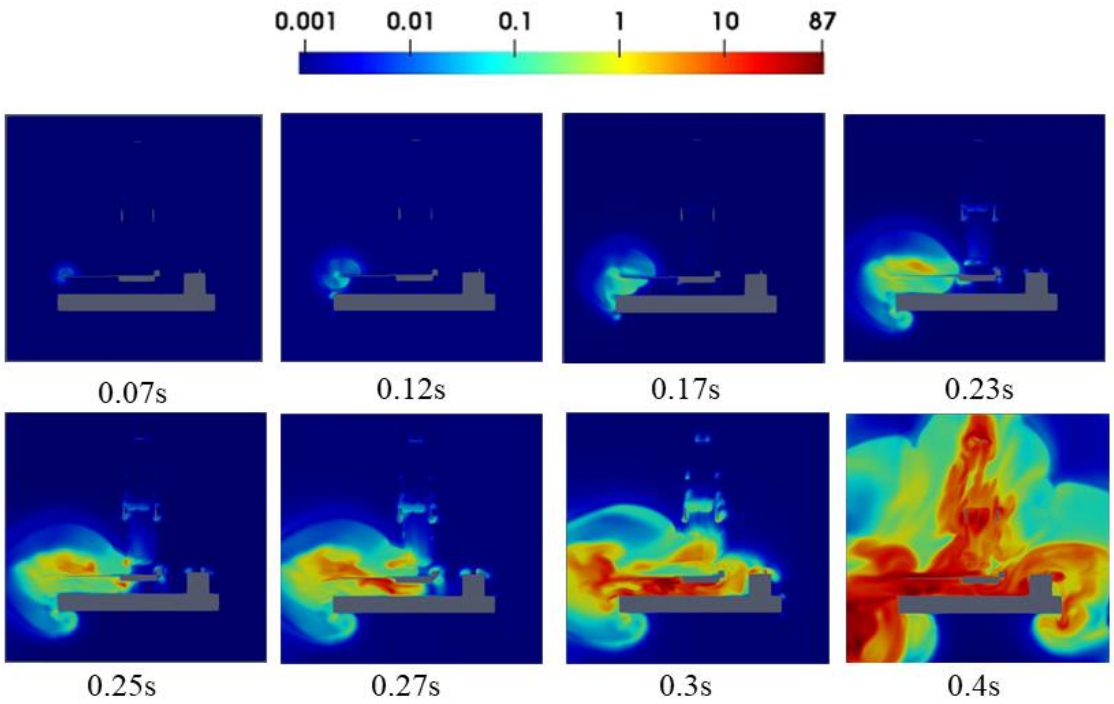

Fig. 14 Turbulence kinetic energy k evolution of XZ slice of the 1st ignition

Fig. 13 demonstrates the flame front evolution of XZ slice of the 1st ignition position. Fig. 14 shows turbulence kinetic energy k evolution of XZ slice of the 1st ignition. Please noting that the turbulence kinetic energy k presents the turbulence generation by flow instabilities and the obstacles and confinements of this semi-submersible platform. From Fig. 13 and Fig. 14, one may see the low level of turbulence kinetic energy k at the initial stage after the ignition, i.e., during t=0.07s to t=0.12s. At this stage, flame propagation is dominated by hydrodynamic instabilities because few obstacles exist around the 1st ignition position. Subsequently, turbulence intensities of flame fronts from directions a and b are enhanced by the front deck of the drilling module. This induces the propagation of flame fronts from direction a and direction b to the drilling module, and both frame fronts arrive at the drilling module at about t=0.25s.

After that, it seems that the confinement between the platform main deck and the drilling module deck in direction a enhances the turbulence intensity more, compared to the congested obstacles of the drilling module in direction b. The flame front becomes closer to the accommodation module in direction a compared to that in direction b from 0.27s to 0.30s. In addition, the flame front of direction a begins to propagate along direction e due to the confinement of the drilling module front wall. Also, the flame front starts to propagate along direction d when the flame front of direction b arrives at the drilling module. Due to the turbulence enhancement of congested obstacles in the drilling module, the flame front in direction d approaches the topside of the derrick more quickly compared to that of directions c and e.

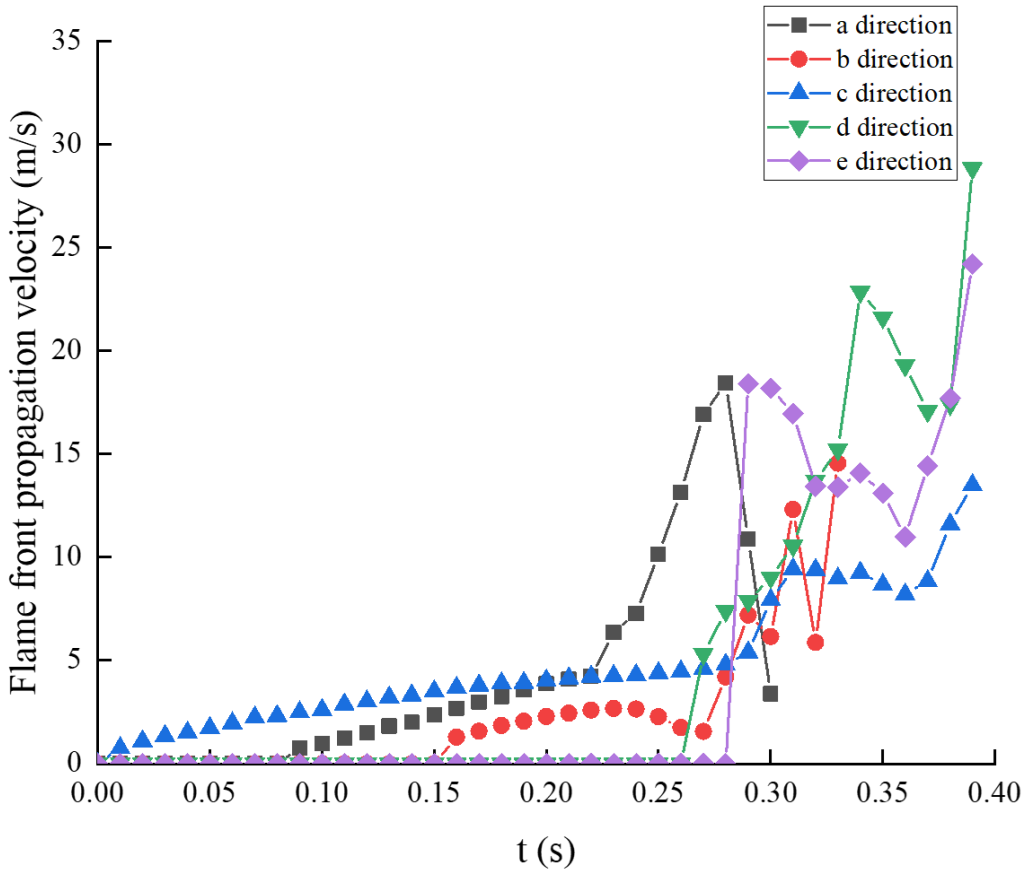

Fig. 15 Flame front propagation velocity of 5 directions under the 1st ignition

Fig. 15 shows flame front propagation velocity of 5 directions under the 1st ignition. From it, one may see that the flame front of direction a propagates with the lower velocity less than 5m/s before t=0.22s, and subsequently, the flame propagation speed is significantly increased to about 18m/s due to the turbulence generation by confinement between the platform main deck and drilling module front deck. Furthermore, due to the confinement of the accommodation module, a significant speed reduction of this flame front propagation is obviously seen from t=0.27s to t=0.30s. Regarding direction b, the flame front propagates at a very low velocity (less than 5m/s) at the initial stage when hydrodynamics instabilities dominate the flame propagation.

After the flame front propagates to the drilling module, the congested obstacles induce a speed acceleration to about 13m/s at t=0.31s. From t=0.31s to t=0.32s, one may see a velocity reduction of flame propagation because the flame front propagates to the area without congested obstacles. Subsequently, an increase in propagation speed can be obviously seen, which may be attributed to the merging of flame fronts from direction b and from direction e. By comparing the propagation velocity between the direction a and direction b, one may see the highest propagation velocity of direction a is larger than that of direction b. This may indicate the confinement between platform main deck and drilling module deck has more significant effect on flame front propagation speed acceleration compared to the congested obstacles of drilling module. In addition, from Fig. 15, one may see the low velocity (less than 5m/s) of flame front propagation in direction c from t=0s to t=0.28s because of hydrodynamic instabilities.

Comparatively, the congested obstacles of the drilling module induce the significant acceleration of

flame front propagation from t=0.26s to 0.40s in direction d. Within this short period, a propagation speed acceleration could also be seen in direction c. This acceleration is thought to be affected by the flame propagation of direction d since there are no obstacles in direction c, and the hydrodynamic instabilities could not induce such great acceleration. In terms of direction e, the initial flame front propagation velocity is very high (about 18 m/s) due to the confinement of the accommodation module. However, between t=0.30s and t=0.36s, a reduction of propagation velocity could be seen because of hydrodynamics instabilities. After t=0.36s, one may see an increase in propagation velocity, which is thought to be induced by the flame propagation of direction d with the relatively faster propagation speed.

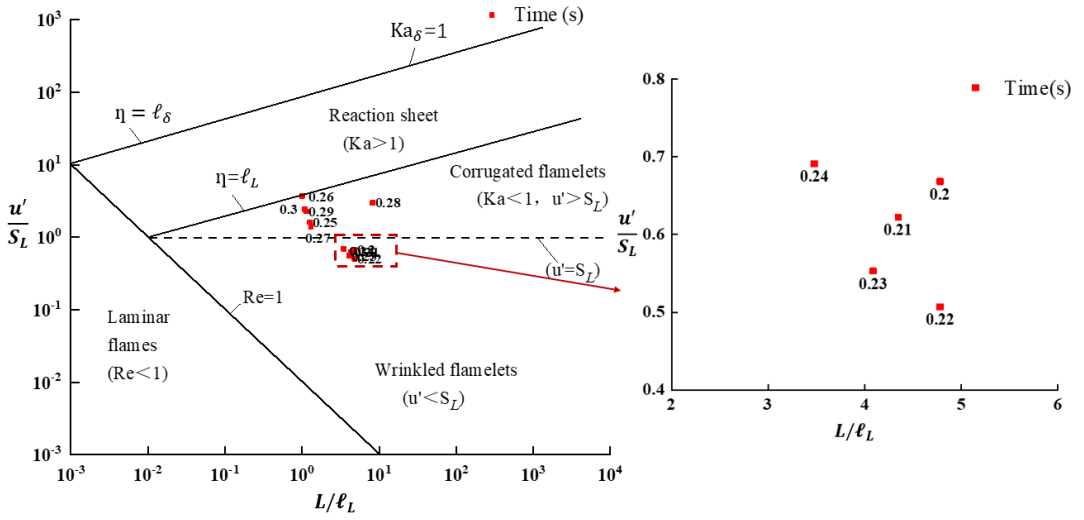

a) a direction

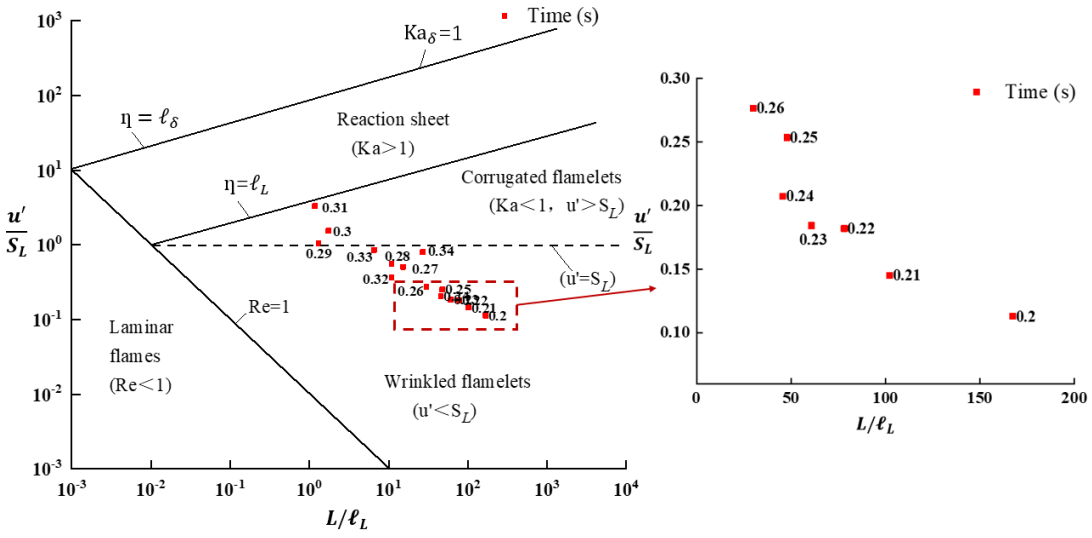

b) b direction

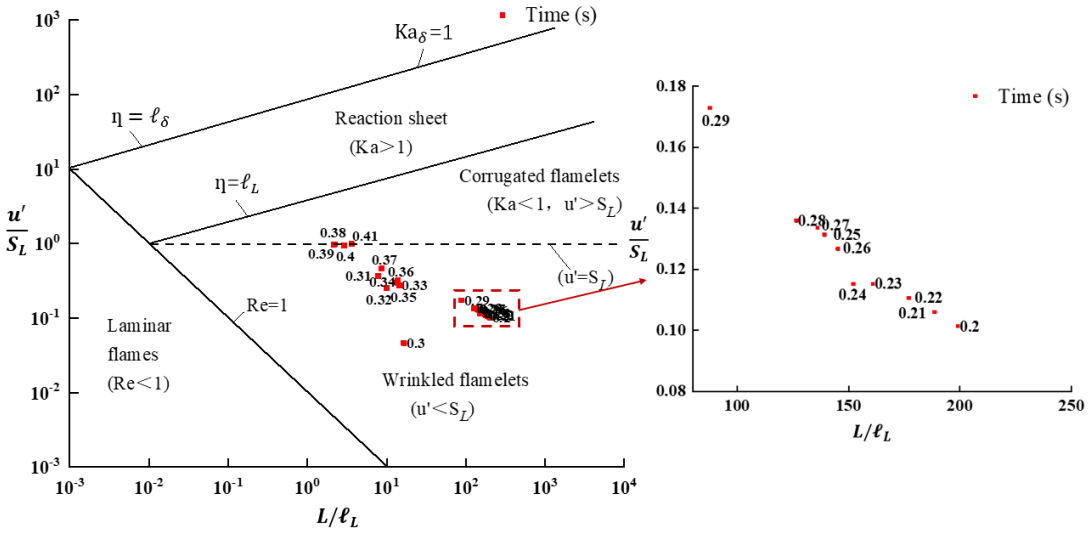

c) c direction

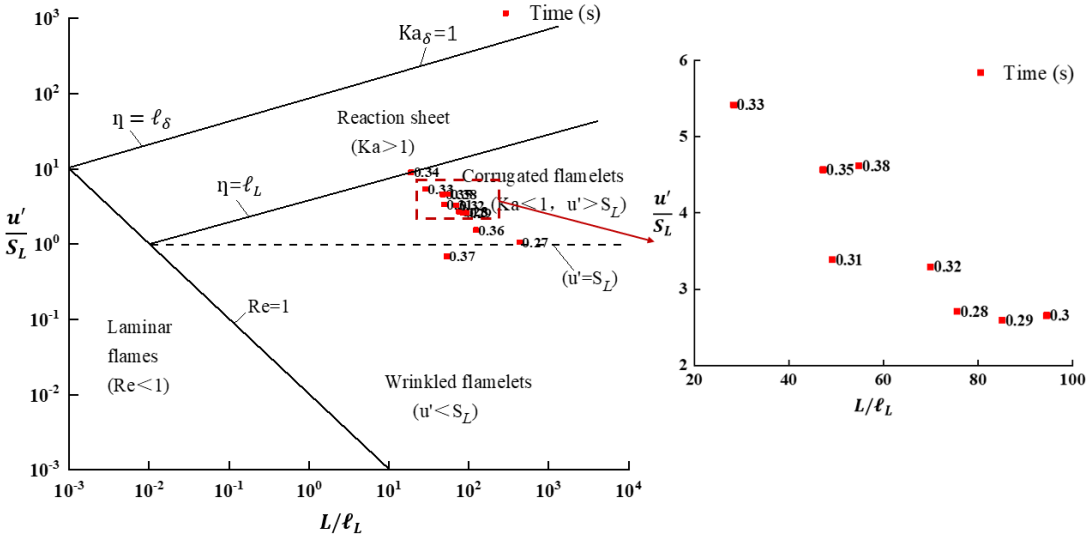

d) d direction

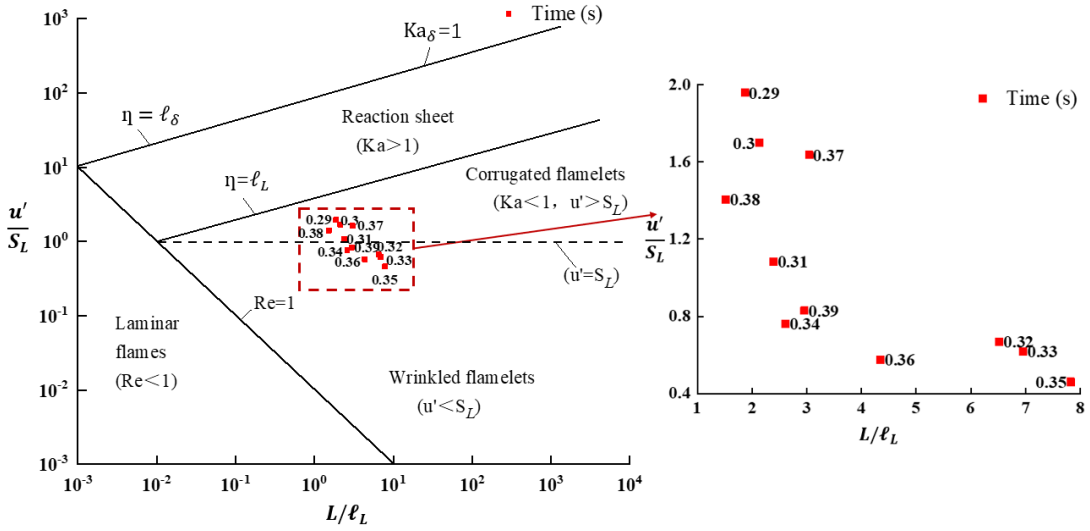

e) e direction

Fig. 16 Flame front mode evolution of 5 directions under the 1st ignition condition[38]. Please noting $u' = (2/3k)^{1/2}$, S_L=0.434m/s for flammable vapor cloud with 4.2% propane concentration, $L = k^{2/3}/\varepsilon$, and ℓ_L is the local grid size.

Fig. 16 is the mode evolution of the flame front along 5 directions under the 1st ignition. From Fig. 16a), one may see the flame front wrinkling of direction a at the initial stage because of the influence of hydrodynamic instabilities. When the flame front propagates to the drilling module at about t=0.25s, we can see the transition of flame front mode from wrinkling flamelets to corrugated flamelets. This transition corresponds to the acceleration of the flame front in direction a, induced by the confinement between the platform main deck and the drilling module deck from about t=0.25s. The transition also occurs in direction b in Fig. 16b) due to the congested obstacles of the drilling module, which contribute to the increase of flame front propagation velocity in direction b, as shown in Fig. 15.

From Fig. 16c), the flame front evolutes as wrinkling flamelets in direction c even though the acceleration of flame front can be seen in Fig. 15. Relatively, due to the congested obstacles of drilling module, the flame front evolutes as corrugated flamelets in direction d as is shown in Fig. 16d). In addition, from Fig. 16e), one may see the corrugated flamelets of direction e at the initial stage due to the confinement of accommodation module. After t=0.30s, a transition of flame front mode from corrugated flamelets to wrinkling flamelets can be seen. This transition corresponds to the velocity reduction of flame front propagation in Fig. 15 after t=0.30s because of hydrodynamic instabilities. After t=0.36s, one may see the flame front becomes corrugated flamelets again from wrinkling flamelets. This second transition corresponds to the acceleration of flame front propagation induced by both hydrodynamic instabilities and the flame propagation of direction d with the relatively higher propagation speed.

(2) The 2nd ignition point

Taking the XY slice of 2nd ignition position as the example to investigate the flame propagation mechanism. Fig. 17 shows the exampled XZ slice, including 4 flame propagation directions, namely a, b, c and d. For direction a, the flame propagation is confined by the obstacles of the drilling module and the accommodation module. For direction b, the front deck of the drilling module exists. For both directions c and d, the flame front would interact with very few unevenly distributed obstacles or confinements. Additional propagation direction, namely direction e is the same as direction d in Fig. 12. In this direction e, the flame propagates through the area of the drilling module containing congested obstacles. Note that all five directions have the same start point with coordinates (1.6, 1.53, 0.75).

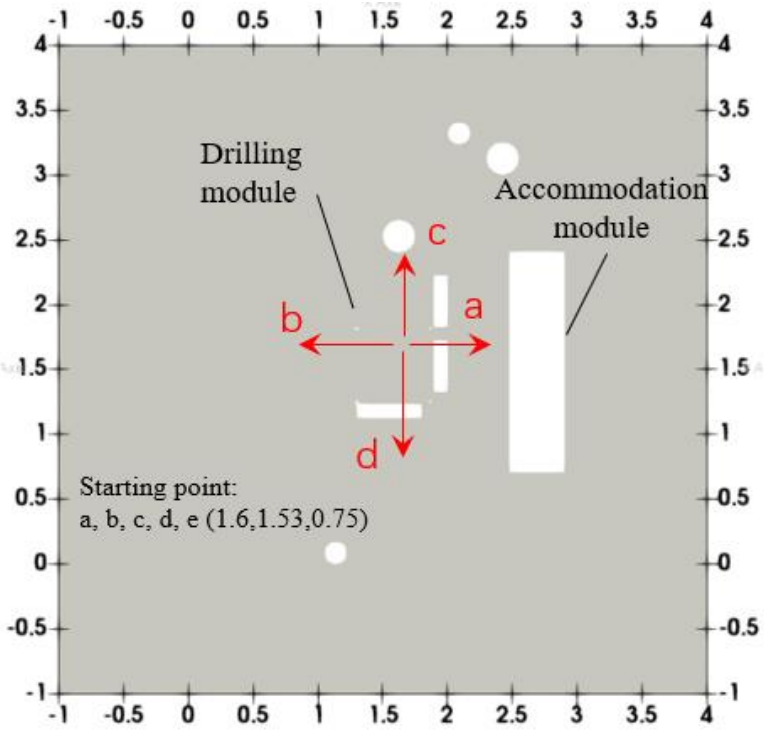

Fig. 17 Exampled directions of flame propagation at XY slice of the 2nd ignition position

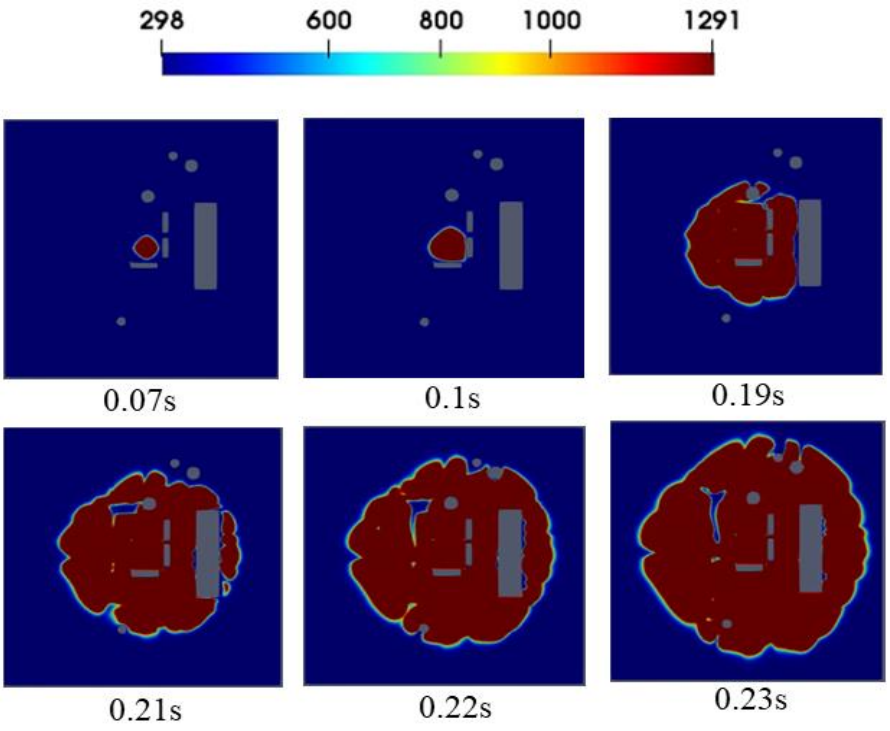

Fig. 18 Flame front propagation of XY slice of the 2nd ignition position

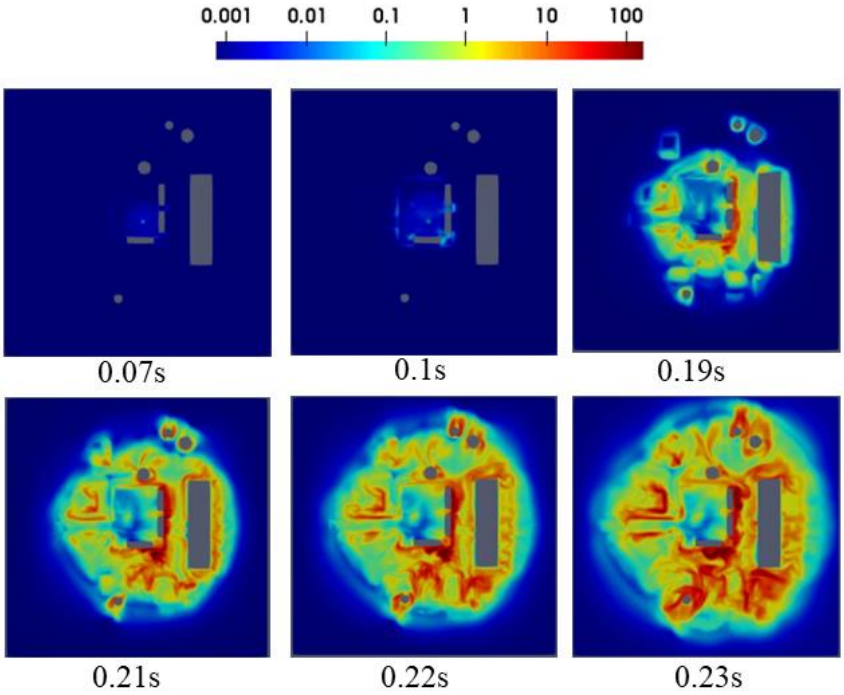

Fig. 19 Turbulence kinetic energy k evolution of XY slice of the 2nd ignition position

Fig. 18 shows the flame front evolution at XY slice of the 2nd ignition position. Fig. 19 is the turbulence kinetic energy k evolution at XY slice of the 2nd ignition position. From Fig. 18 and Fig. 19, one may see the flame front propagates spherically due to the effects of hydrodynamic instabilities, which induce a low level of turbulence kinetic energy k at the initial stage after ignition. At about t=0.10s, the flame front approaches the obstacles of the drilling module in direction a and d. These obstacles generate more significant level of turbulence kinetic energy k compared to that in direction b and c even though the interaction of flame with drilling module deck of direction b and flame with circular obstacle of direction c could also induce a certain level of turbulence kinetic energy k. Furthermore, the flame front propagation of direction a is obstructed by accommodation module from about t=0.19s. The confinement of the accommodation module induces the flame front to propagate along the front wall of the accommodation module and merge with the flame front in direction c and d from about t=0.19s. This seems to generate a great level of turbulence kinetic energy k in both direction c and d. In direction b, after about t=0.19s, there seems to be a high level of turbulence kinetic energy k at the flame front, which may be attributed to the interaction of flame front with the drilling module front deck as well as the confined flame propagation in direction a.

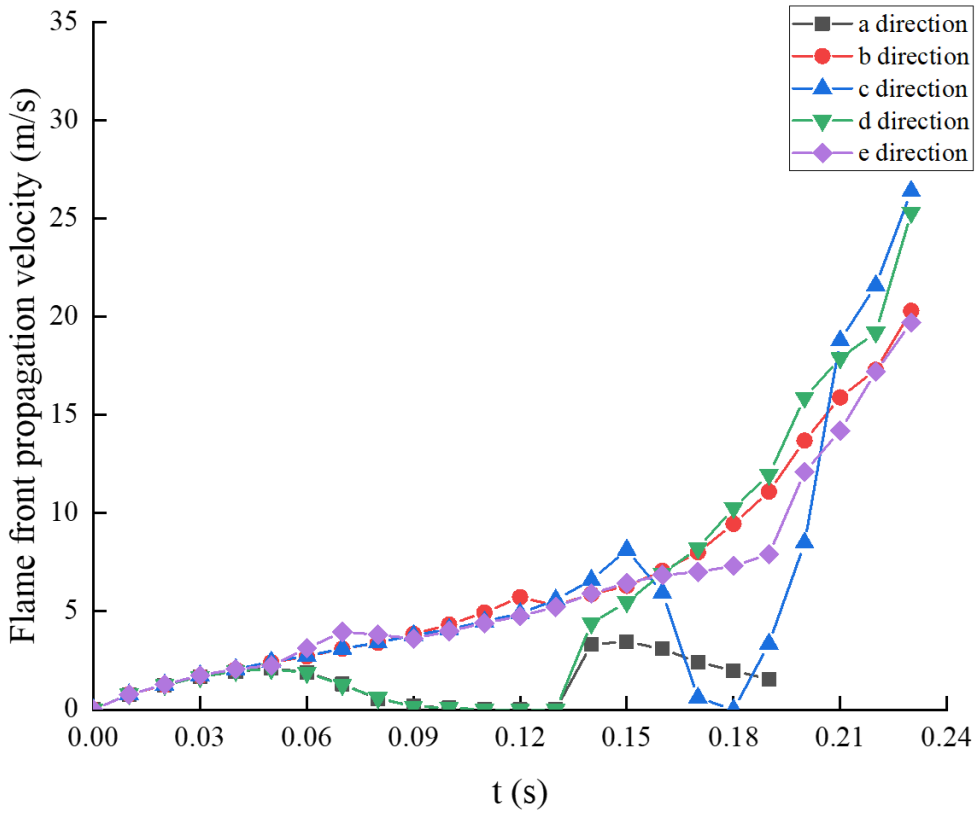

Fig. 20 Flame front propagation velocity of 5 directions under the 2nd ignition

Fig. 20 shows flame front propagation velocity of 5 directions under the 2nd ignition. The increase of flame front propagation velocity in direction a and direction d before t=0.50s and the subsequent decrease from t=0.50s to t=0.13s. This velocity reduction may be attributed to the confinement of obstacles from the drilling module. After t=0.13s, an increase of flame front propagation velocity in direction a due to the obstacles-induced turbulence effects. However, due to the confinement of the accommodation module, this propagation velocity decreases again until the flame front approaches the front wall of the accommodation module at t=0.19s. In terms of directions b, c and d, the flame front propagation velocity increases with a relatively gentle slope before about t=0.15s, which may be attributed to the turbulence generation by hydrodynamic instabilities and few obstacles in respective directions. However, one may see the subsequent velocity increase with a steep scope after t=0.15s. This rapid growth period of propagation velocity exists in directions b, c and d. It also corresponds to that when the propagation velocity decreases in direction a due to the confinement of the accommodation module.

Considering few obstacles exist in directions b, c and d, it is thought that the confinement of the accommodation module contributes to this significant increase in propagation velocity. For example, as is illustrated in Fig. 18 and Fig. 19, the front wall of the accommodation module induces the flame front of direction a to propagate along direction c and direction a from about t=0.19s. Then, the interaction between the original flame front of direction c and the confined flame front seems to generate a great level of turbulence kinetic energy k, which contributes to the great velocity increasement. In terms of direction e, the acceleration of flame front propagation velocity is mainly induced by the congested obstacles from the drilling module. However, one may also see the propagation speed increases with a relatively steep slope after t=0.19s, which is thought to be affected by the flame

propagation with direction changed by the confinement of the accommodation module, in addition to the congestions of the drilling module.

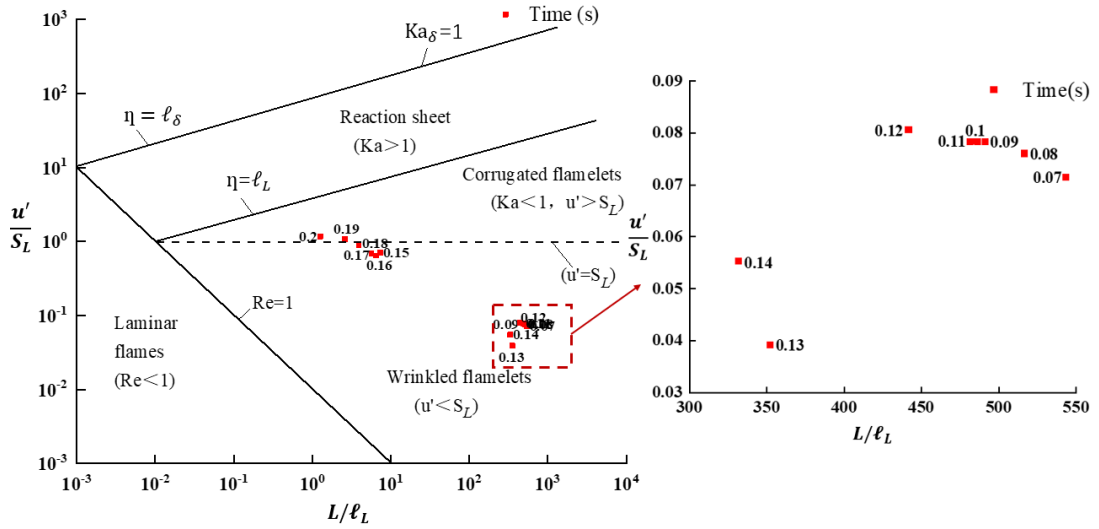

a) a direction

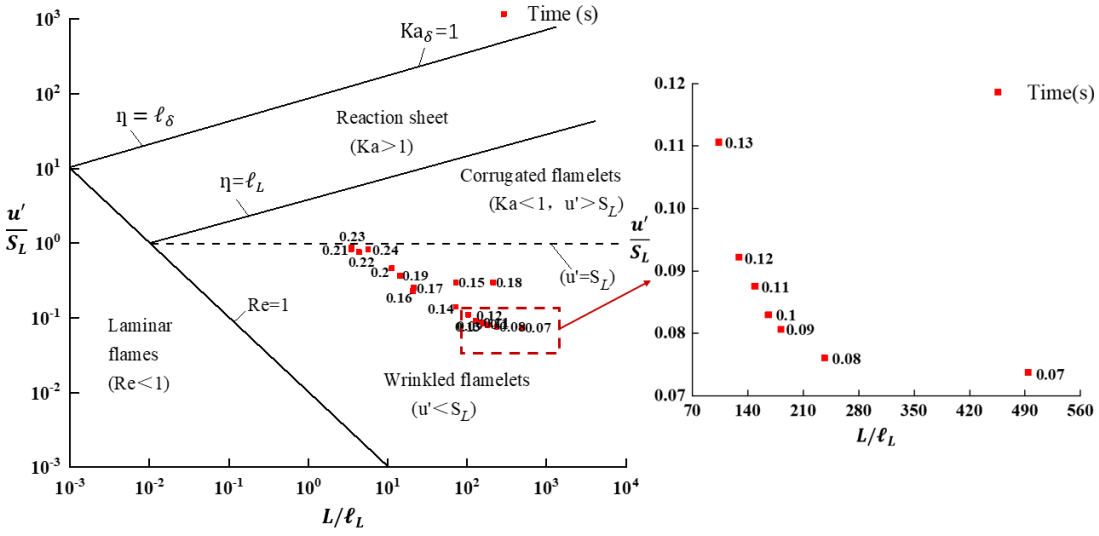

b) b direction

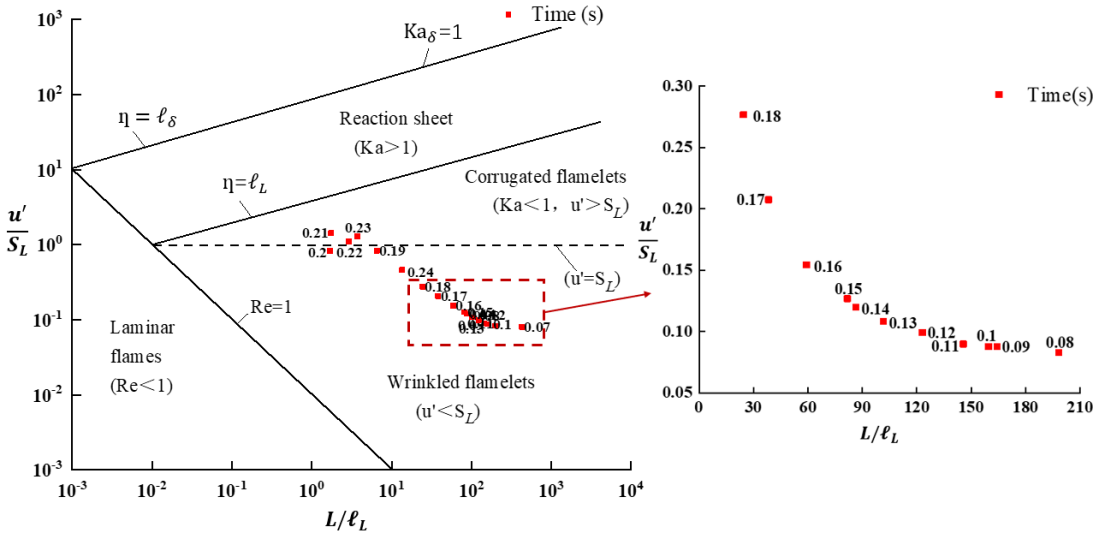

c) c direction

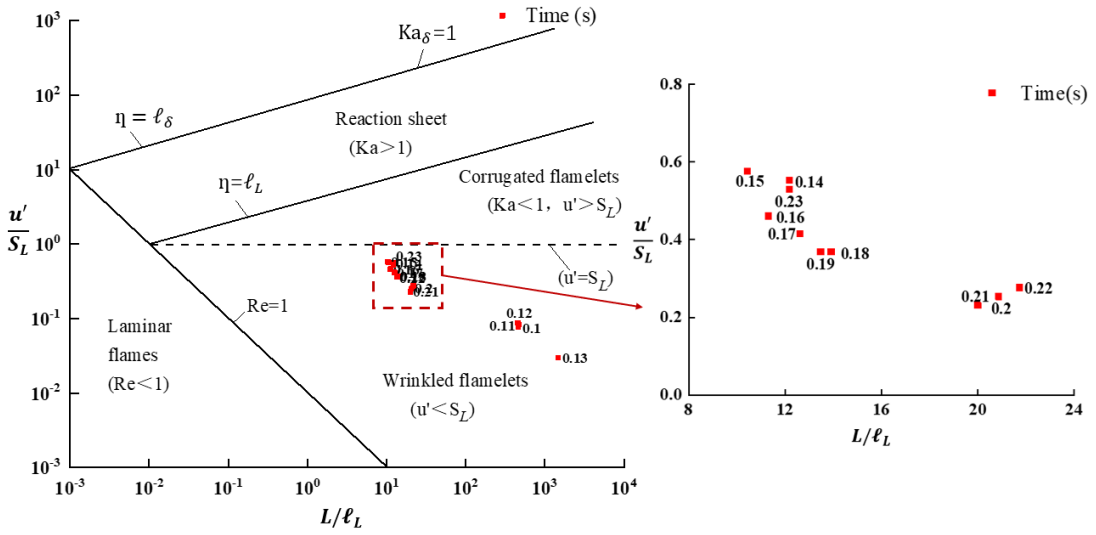

d) d direction

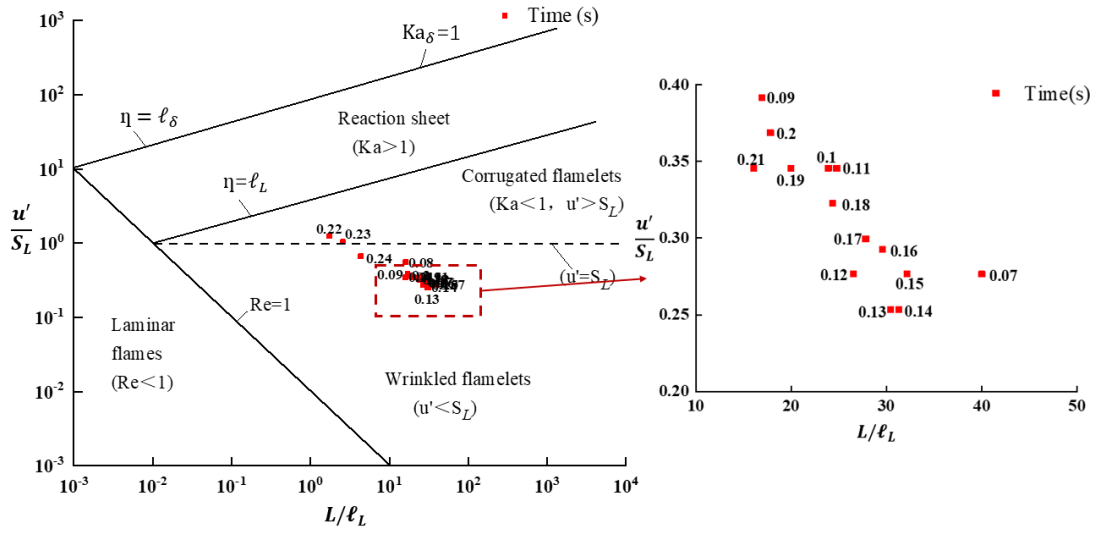

e) e direction

Fig. 21 Flame front mode evolution of 5 directions under the 2nd ignition[38]. Please noting $u' = (2/3k)^{1/2}$, S_L=0.434m/s for flammable vapor cloud with 4.2% propane concentration, $L = k^{2/3}/\varepsilon$, and ℓ_L is the local grid size.

Fig. 21 shows the mode evolution of flame front along five directions under the 2nd ignition. From Fig. 21a), one may see the flame front is wrinkled in direction a at the initial stage, despite the effects of obstacles from the drilling module. Subsequently, because of the confinement of the accommodation module, the transition of flame front mode from wrinkling flamelets to corrugated flamelets can be seen at about t=0.19s. This transition corresponds to the duration of the reduction of flame front propagation velocity in direction a as is shown in Fig. 20. In terms of direction b, no transition occurs even though the mode of flame front becomes closed to be corrugated flamelets after t=0.19s during which the flame front propagation velocity is enhanced by the confinement of accommodation module. From Fig. 21c), one may see the transition of flame front mode in direction c after about t=0.19s. However, for direction d, no transition of flame front mode exists after about t=0.19s, although the confinement of the accommodation module contributes to this flame front propagation acceleration. This may be attributed to fewer obstacles at the end of direction d compared to direction c. From Fig. 21e), one may see at the initial stage, the flame front is wrinkled in direction e. After interacting with congested obstacles of the drilling module, the flame front becomes corrugated after about t=0.21s in addition to the contribution

from the accommodation module confinement.

4.2. Overpressure distribution characteristic

(1) The 1st ignition point

Taking the XZ slice of 1st ignition position in Fig. 12 as the example to demonstrate the overpressure propagation and distribution. 5 propagation directions same with that in Fig. 12 were also used, and from each direction, monitors were sampled to analyze the distribution characteristic of maximum overpressure.

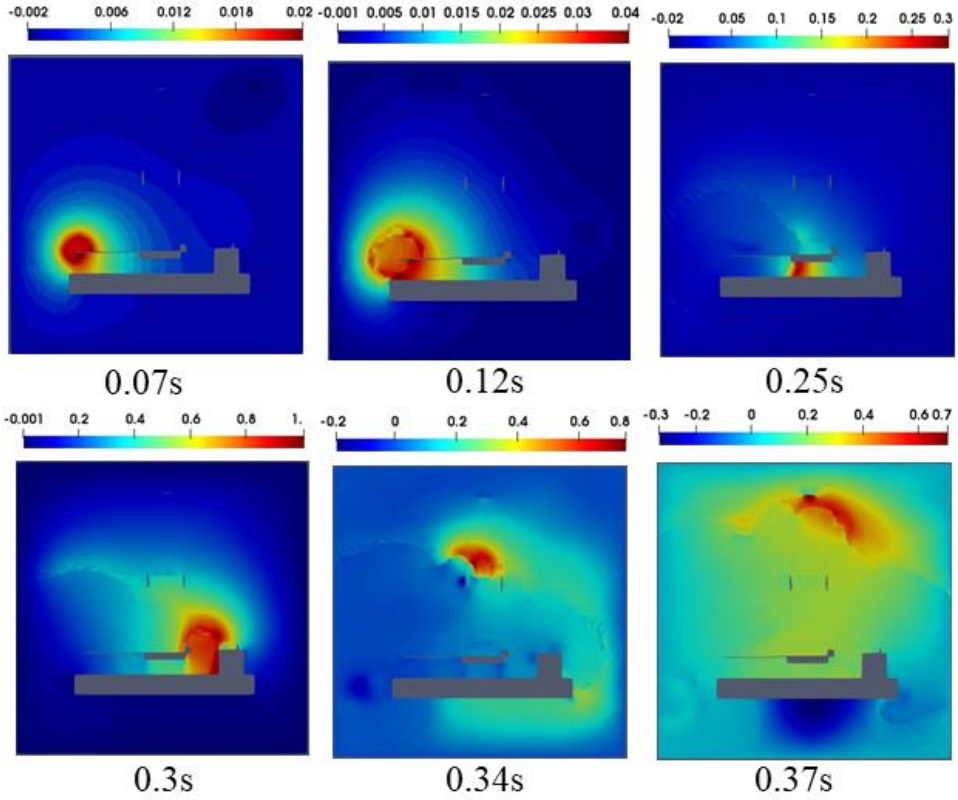

Fig. 22 Overpressure evolution at XZ slice of the 1st ignition position

Fig. 22 shows overpressure evolution at exampled XZ slice of the 1st ignition position. From it, one may see at the initial stage from t=0.70s to t=0.12s, the blast wave front propagates spherically, and the corresponding overpressure values from different directions are small and similar. This is because at this initial stage, the flame propagation is dominated by hydrodynamic instabilities due to the fact that few obstacles exist, as is illustrated in Section 4.1. Subsequently, due to the obstructed effect of the front deck of the drilling module, the overpressure values at the front of directions a and b become relatively larger compared to other directions. After about t=0.25s, due to the confinement between the platform main deck and the drilling module deck, the overpressure at the front of direction a becomes larger compared to that of direction b. Also, the maximum overpressure of 1 kPa in direction a can be seen at the front wall of the accommodation module at about t=0.30s. This maximum overpressure of 1 kPa is relatively larger than that induced by obstacles of the drilling module in direction b. In addition, at t=0.30s, one may see the large local overpressures of about 0.6 kPa are distributed at the top side of the accommodation module and the back side of the drilling module. These local overpressures are thought to be induced by the combination of the flame fronts of direction d and direction b. After that, one may see the larger local overpressures of the front side of derrick at t=0.30s, the middle of derrick at t=0.34s, and the back side of derrick at t=0.37s. These local overpressures are thought to be generated by the

combined effects of the obstacle-accelerated flame front in direction c and the hydrodynamics instabilities-dominated flame front in direction b and e.

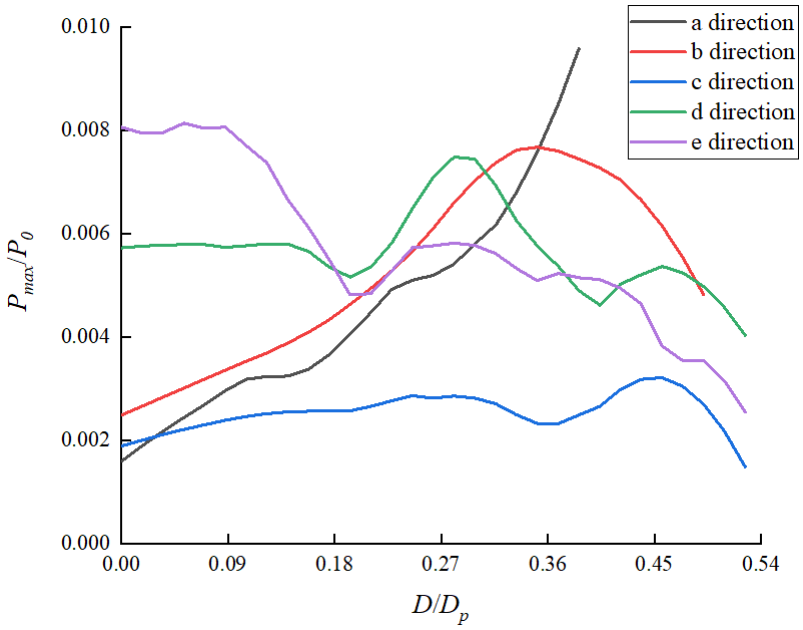

Fig. 23 Dimensionless maximum overpressure versus dimensionless distance from 5 directions under the 1st ignition

Fig. 23 shows the dimensionless maximum overpressure versus dimensionless distance from 5 directions under the 1st ignition. Note that the dimensionless maximum overpressure equals to the maximum overpressure/standard atmospheric pressure (P_{max} / P_0). The dimensionless distance was calculated by the distance D from the start point of each direction divided by $D_p = \sqrt{3.09^2 + 3.29^2 + 3.46^2}$ where 3.09 m, 3.29 m, 3.46 m are the length, width, and height of this offshore platform. From it, one may see with the increase of dimensionless distance in direction a, the dimensionless maximum overpressure increases, and the largest value = 0.010 exists at the end of direction a, i.e., at the front wall of the accommodation module. In terms of direction b, the dimensionless maximum overpressure first increases and then decreases with increasing the dimensionless distance.

The larger dimensionless maximum overpressures are located at the back side of the drilling module, which is thought to be induced by the combination of the flame fronts of direction d and direction b. For direction c, the dimensionless maximum overpressures are relatively smaller compared to other directions, even though the obstacle-accelerated flame front of direction d contributes to the acceleration of hydrodynamics instabilities-dominated flame front propagation. Furthermore, one may see the largest dimensionless maximum overpressure of about 0.008 is located at the middle part of the derrick due to the combined effects of the obstacle-accelerated flame front of direction d and the hydrodynamics instabilities-dominated flame front in directions b and e. For direction e, the larger dimensionless maximum overpressure can be seen when the dimensionless distance equals to 0.09, i.e., the position close to the top side of the accommodation module and the back side of the drilling module, which are thought to be induced by the combination of the flame fronts of direction d and direction b.

(2) The 2nd ignition point

Taking the XY slice of 2nd ignition position in Fig. 17 as the example to demonstrate the overpressure

propagation and distribution. Five directions were selected in which directions a, b, c and d were the same, while direction e was the same as direction d in Fig. 12.

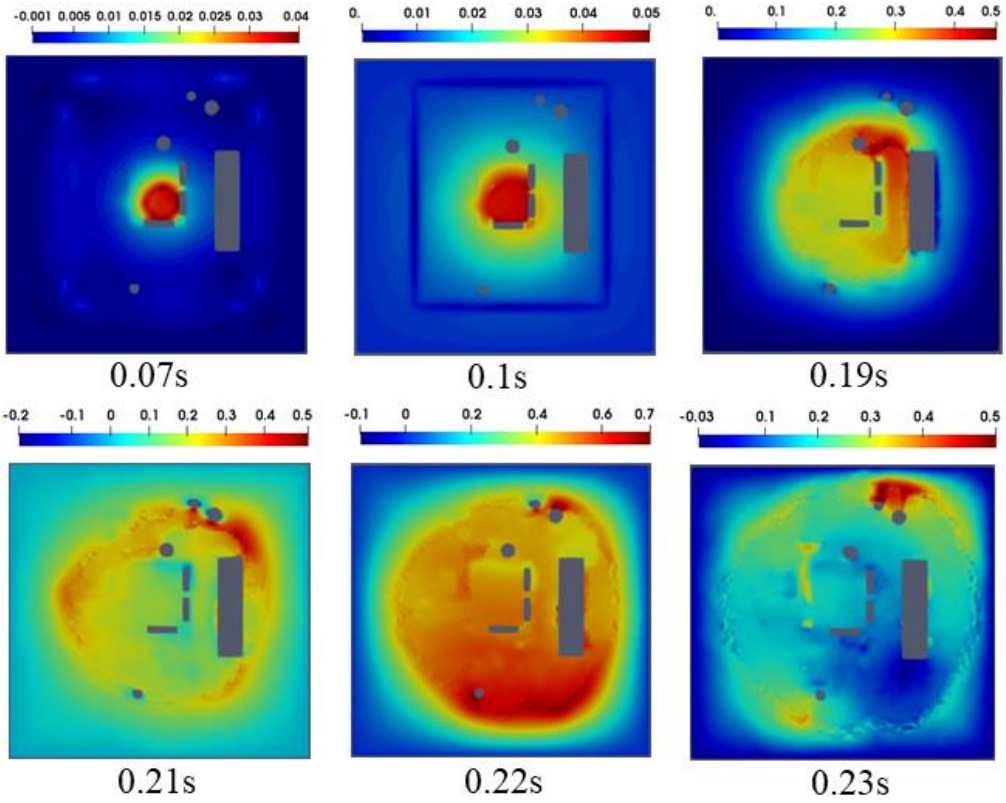

Fig. 24 Overpressure evolution at XY slice of the 2nd ignition position

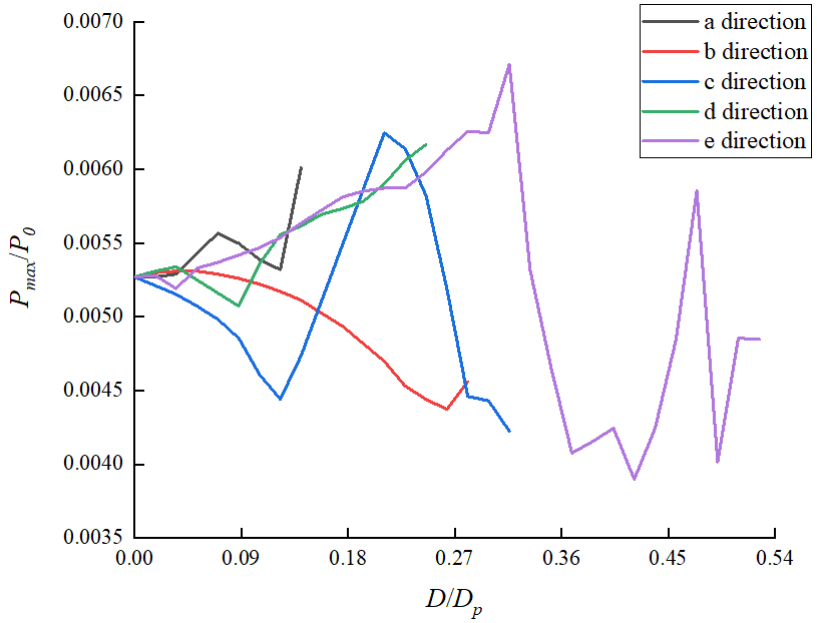

Fig. 25 Dimensionless maximum overpressure versus dimensionless distance from 5 directions under the 2nd ignition

Fig. 24 demonstrates overpressure evolution at XY slice of the 2nd ignition position. From it, one may see the blast wave front propagates spherically, and the overpressures at the front from different directions are similar at the initial stage from t=0.07s to t=0.10s. After that, due to the obstacles of the

drilling module and the confinement of accommodation module front wall, the overpressure at the blast wave front of direction a becomes larger compared to that of other directions. Between t=0.19s and t=0.21s, one may see the larger local overpressures exist, which are thought to be induced by the interaction between the original flame front of direction c and the confined flame front by the accommodation module front wall. Furthermore, at t=0.22s, both the right and left edges of the offshore platform have relatively larger local overpressures. The occurrence of larger local overpressures corresponds to the acceleration of flame front propagation with flame front mode transition in directions c and d. In addition, the existence of obstacles at the right edge of the offshore platform has the potential to enhance the local overpressure, e.g., the larger overpressure of 0.6 kPa at the right edge when t=0.23s.

Fig. 25 shows the dimensionless maximum overpressure versus dimensionless distance from 5 directions under the 2nd ignition. From it, one may see the largest dimensionless maximum overpressure of 0.0060 at the end of direction a, i.e., at the front wall of the accommodation module. For direction b, the dimensionless maximum overpressure decrease with increasing the dimensionless distance, and the largest values are distributed at the drilling module. Furthermore, in terms of direction c, the largest dimensionless maximum overpressure can be seen under dimensionless distance=0.21, i.e., the position is located at the right edge of this platform where round obstacles exist. This largest value is thought to be induced by the combined effects of flame front propagations of direction c and direction a confined by the accommodation module and obstacles. In addition, the largest dimensionless maximum overpressure is located at the left edge of this platform in direction d, which is thought to be induced by the combination of flame front propagations of direction c and direction a confined by the accommodation module. Note that the combination effects also contribute to the acceleration of flame front propagation with flame mode transition in directions c and d as is illustrated in Section 4.1. In terms of direction e, one may also see the largest dimensionless maximum overpressure is located at the middle of the drilling derrick due to the combined effects of the obstacle-accelerated flame front and the hydrodynamics instabilities-dominated flame front.

5. Discussions

Despite detailed experimental and numerical outcomes in this work, its key assumptions and limitations shall be claried. Firstly, this study did not apply the PDR-based solver, such as STOKES and PDRFoam, which have been validated to be excellent solutions with both computational accuracy and efficiency, especially for large-scale gas explosion prediction with complex geometries. The better one between Xifoam and PDR-based solver for gas explosion simulation from a semi-submersible platform is still unknown, which is worth future investigation. In terms of Xifoam solver, a high-quality domain grid should be configured, and the turbulent and combustion coefficients are required to be carefully re-calibrated to capture flame propagation, especially with small-scale geometries. This indicates that the application of Xifoam solver requires more computational resources, especially for large-scale applications, compared to the PDR-based solver.

Additionally, the high-speed camera of the experimental system cannot capture the explosion flame front clearly due to unavoidable disturbance factors of the outdoor experimental site. Thus, it is difficult to conduct precise comparisons between numerically predicted and experimental flame propagations. Future works are expected to improve reliable measurements and accordingly analyze different gas

explosion scenarios by experimentally and numerically configuring different ignition positions, congestion levels, flammable gas components, etc.

6. Conclusions

This study investigated the flame evolution mechanism and overpressure distribution characteristic of gas explosion from a semi-submersible platform. A 3D numerical model was developed by using Xifoam solver. Premixed propane-air mixture explosion experiments from a medium-scale semi-submersible platform were conducted to validate the accuracy of the numerical model. Numerical simulations whose configurations were the same as the experimental setup were conducted. We found that:

(1) Two flame regimes, namely wrinkling flame and corrugated flame, occur. The congested obstacles of the drilling module, the confinement between the drilling module deck and the topside main deck, and the confinement of the accommodation module play significant roles in the transition of flame regimes.
(2) The hydrodynamics instability-dominated flame propagation can be accelerated by the flame propagation dominated by the congested obstacles of the drilling module. This acceleration leads to the transition of the flame regime and the generation of larger local overpressure.
(3) For a long-distance ignition, the largest overpressure peaks at the accommodation module of the offshore platform. The combination of flame fronts dominated by obstacles of the drilling module and confined by the accommodation module front wall induces larger overpressure peaks at the middle and back sides of the drilling module.
(4) The ignition of the drilling module causes a larger overpressure peak at both the left and right edges of the main deck of the offshore platform. The combination of flame front propagation dominated by obstacles at both the left and right edges of the offshore platform and confined by the accommodation module front wall induces the larger overpressure peak.
(5) For both ignition positions, the middle part of the drilling derrick has the larger overpressure peak., which may be attributed to the combination of flame front propagation induced by obstacles of the drilling module and dominated by hydrodynamics instabilities.

These conclusions provide a valuable theoretical foundation to help design mitigation measures for gas explosions on semi-submersible platforms.

Acknowledgments

This study was supported by National Natural Science Foundation of China (Project No.: 52101341). Natural Science Foundation of Shandong Province (Project No.: ZR2020KF018). China Postdoctoral Science Foundation Funded Project (Project No.: 2019M662469). Qingdao Science and Technology Plan (Project No.: 203412nsh). Key Project of Natural Science Foundation of Shandong Province (Project No.: ZR2020KF018). The authors would like to acknowledge partially support of the Hong Kong Research Grants Council (T22-505/19-N).

References

[1] J. Shi, J. Li, H. Hao, T.M. Pham, Y. Zhu, G. Chen, Robust data-driven model to study dispersion of vapor

cloud in offshore facility, Ocean Engineering, 161 (2018) 98-110.
[2] J. Shi, Y. Zhu, D. Kong, F. Khan, J. Li, G. Chen, Stochastic analysis of explosion risk for ultra-deep-water semi-submersible offshore platforms, Ocean Engineering, 172 (2019) 844-856.
[3] J. Shi, J. Li, F. Khan, Y. Chang, Y. Zhu, G. Chen, Explosion risk-based water spray mitigation analysis of ultra-deep-water semi-submersible platforms, Ocean Engineering, 239 (2021) 109716.
[4] S. Park, B. Jeong, B.S. Lee, S. Oterkus, P. Zhou, Potential risk of vapour cloud explosion in FLNG liquefaction modules, Ocean Engineering, 149 (2018) 423-437.
[5] T. Baalisampang, R. Abbassi, V. Garaniya, F. Khan, M. Dadashzadeh, Review and analysis of fire and explosion accidents in maritime transportation, Ocean Engineering, 158 (2018) 350-366.
[6] S. Lee, Quantitative risk assessment of fire & explosion for regasification process of an LNG-FSRU, Ocean Engineering, 197 (2020) 106825.
[7] F. Han, X. Hongxiang, T. Wenyong, Characteristics of gas explosion loads and structural responses of blast wall on FPSO, Marine Structures, 87 (2023) 103315.
[8] M. Dadashzadeh, R. Abbassi, F. Khan, K. Hawboldt, Explosion modeling and analysis of BP Deepwater Horizon accident, Safety Science, 57 (2013) 150-160.
[9] C. Selby, B. Burgan, Blast and fire engineering for topside structures-Phase 2. Final summary report, Steel Construction Institute, England, UK, (1998).
[10] B.J. Kim, J.K. Seo, J.H. Park, J.S. Jeong, B.K. Oh, S.H. Kim, C.H. Park, J.K. Paik, Load characteristics of steel and concrete tubular members under jet fire: an experimental and numerical study, Ocean Engineering, 37 (2010) 1159-1168.
[11] B.J. Kim, J. Yoon, G. Yu, H. Ryu, Y. Ha, J. Paik, Heat flow analysis of an FPSO topside model with wind effect taken into account: A wind-tunnel test and CFD simulation, Ocean Engineering, 38 (2011) 1130-1140.
[12] J.H. Kim, C.K. Kim, M.S. Islam, S.I. Park, J.K. Paik, A study on methods for fire load application with passive fire protection effects, Ocean Engineering, 70 (2013) 177-187.
[13] J.K. Paik, J. Czujko, J.H. Kim, S.I. Park, S. Islam, D.H. Lee, A new procedure for the nonlinear structural response analysis of offshore installations in fires, SNAME Maritime Convention, SNAME, 2013, pp. D011S005R009.
[14] J.M. Sohn, S.J. Kim, B.H. Kim, J.K. Paik, Nonlinear structural consequence analysis of FPSO topside blastwalls, Ocean Engineering, 60 (2013) 149-162.
[15] B. Hjertager, K. Fuhre, M. Bjørkhaug, Gas explosion experiments in 1: 33 and 1: 5 scale offshore separator and compressor modules using stoichiometric homogeneous fuel/air clouds, Journal of loss prevention in the process industries, 1 (1988) 197-205.
[16] J. Puttock, F. Walter, D. Chakraborty, S. Raghunath, P. Sathiah, Numerical simulations of gas explosion using Porosity Distributed Resistance approach Part −1: Validation against small-scale experiments, Journal of Loss Prevention in the Process Industries, 75 (2022).
[17] A. Van den Berg, A. Mos, Research to improve guidance on separation distance for the multi-energy method (RIGOS), HSE2005.
[18] W. Mercx, D. Johnson, J. Puttock, Validation of scaling techniques for experimental vapor cloud explosion investigations, Process Safety Progress, 14 (1995) 120-130.
[19] P. Snowdon, J. Puttock, E. Provost, T. Cresswell, J. Rowson, R. Johnson, A. Masters, S. Bimson, Critical design of validation experiments for vapour cloud explosion assessment methods, Proceedings of International Conference and Workshop on Modeling the Consequence of Accidental Releases of Hazardous Materials, San Francisco, 1999, pp. 831-849.
[20] J. Shi, J. Li, H. Hao, T.M. Pham, Y. Zhu, G. Chen, Vented gas explosion overpressure prediction of obstructed cubic chamber by Bayesian Regularization Artificial Neuron Network – Bauwens model, Journal of Loss Prevention in the Process Industries, 56 (2018) 209-216.
[21] J. Shi, J. Li, H. Hao, Y. Zhu, G. Chen, An integrated model for vent area design of hydrocarbon-air mixture

explosion inside cubic enclosures with obstacles, Journal of Loss Prevention in the Process Industries, 57 (2019) 61-72.
[22] J. Li, G. Ma, H. Hao, Y. Huang, Optimal blast wall layout design to mitigate gas dispersion and explosion on a cylindrical FLNG platform, Journal of Loss Prevention in the Process Industries, 49 (2017) 481-492.
[23] J. Li, G. Ma, H. Hao, Y. Huang, Gas explosion analysis of safety gap effect on the innovating FLNG vessel with a cylindrical platform, Journal of Loss Prevention in the Process Industries, 44 (2016) 263-274.
[24] H. Fang, H. Xue, W. Tang, Blast wave propagation characteristics in FPSO: Effect of cubical obstacles, Ocean Engineering, 250 (2022) 111022.
[25] K. Kang, X. Wang, J. Wang, W. Shi, Y. Sun, M. Chen, A Critical Review of a Computational Fluid Dynamics (CFD)-Based Explosion Numerical Analysis of Offshore Facilities, Archives of Computational Methods in Engineering, 29 (2022) 4851-4870.
[26] D.S.N. Abg Shamsuddin, A.F. Mohd Fekeri, A. Muchtar, F. Khan, B.C. Khor, B.H. Lim, M.I. Rosli, M.S. Takriff, Computational fluid dynamics modelling approaches of gas explosion in the chemical process industry: A review, Process Safety and Environmental Protection, 170 (2023) 112-138.
[27] T.D. Ferreira, R.G. Santos, S.S.V. Vianna, A coupled finite volume method and Gilbert–Johnson–Keerthi distance algorithm for computational fluid dynamics modelling, Computer Methods in Applied Mechanics and Engineering, 352 (2019) 417-436.
[28] T.D. Ferreira, S.S.V. Vianna, The Gilbert Johnson Keerthi distance algorithm coupled with computational fluid dynamics applied to gas explosion simulation, Process Safety and Environmental Protection, 130 (2019) 209-220.
[29] T.D. Ferreira, S.S.V. Vianna, Collision of convex objects for calculation of porous mesh in gas explosion simulation, Journal of Loss Prevention in the Process Industries, 69 (2021).
[30] T.L.S. Quaresma, T.D. Ferreira, S.S.V. Vianna, A hybrid BML-fractal approach for the mean reaction rate modelling of accidental gas explosions in partially confined obstructed geometries, Process Safety and Environmental Protection, 152 (2021) 414-426.
[31] T.L.S. Quaresma, T.D. Ferreira, S.S.V. Vianna, Alternative approaches to the reaction rate modelling in gas explosion simulation using STOKES, Journal of Loss Prevention in the Process Industries, 74 (2022).
[32] M. Dhiman, A. Zambare, P. Sathiah, V.D. Narasimhamurthy, CFD simulations of vapour cloud explosions using PDRFoam, Journal of Loss Prevention in the Process Industries, 85 (2023).
[33] Z. Li, L. Chen, H. Yan, Q. Fang, Y. Zhang, H. Xiang, Y. Liu, S. Wang, Gas explosions of methane-air mixtures in a large-scale tube, Fuel, 285 (2021).
[34] K. Gao, Z. Liu, C. Wu, J. Li, K. Liu, Y. Liu, S. Li, Effect of low gas concentration in underground return tunnels on characteristics of gas explosions, Process Safety and Environmental Protection, 152 (2021) 679-691.
[35] C.M.R. Vendra, J.X. Wen, Numerical modelling of vented lean hydrogen deflagations in an ISO container, International Journal of Hydrogen Energy, 44 (2019) 8767-8779.
[36] V.C. Madhav Rao, P. Sathiah, J.X. Wen, Effects of congestion and confining walls on turbulent deflagrations in a hydrogen storage facility-part 2: Numerical study, International Journal of Hydrogen Energy, 43 (2018) 15593-15621.
[37] B.J. Arntzen, Modelling of turbulence and combustion for simulation of gas explosions in complex geometries, (1998).
[38] R. Cant, E. Mastorakos, An introduction to turbulent reacting flows, Imperial College Press, 2008.